Commun. Comput. Phys.
doi: 10.4208/cicp.OA-2024-0080

Vol. **38**, No. 1, pp. 1-36
July 2025

# A Simple Strategy for Multi-Material Diffusion and Its Application to Three-Temperature Multi-Material Flows

B. Manach-Pérennou[1], R. Chauvin[2], S. Guisset[3,*] and J.-P. Perlat[1]

[1] *CEA, DAM, DIF, 91297 Arpajon, France.*
[2] *CEA, DES, IRESNE, Cadarache, 13108 Saint-Paul-lez-Durance, France.*
[3] *CEA, DAM, CESTA, 33116 Le Barp, France.*

Communicated by Kun Xu

Received 5 April 2024; Accepted (in revised version) 1 November 2024

**Abstract.** This work is devoted to the numerical approximation of three-temperature multi-material hydrodynamics. Such systems are subject to stiff phenomena which require specific care during the discretization. In particular, the so-called discrete equation method is here applied to the radiation transport, in the optically-thick limit. This strategy is shown to be accurate in the presence of in-cell interfaces while being simpler than standard interface reconstruction techniques. It is then incorporated into a three-temperature multi-material scheme whose implicit temporal discretization is based on convex combinations. Stiff test cases eventually establish the scheme's robustness.

**AMS subject classifications**: 52B10, 65D18, 68U05, 68U07

**Key words**: Numerical scheme, diffusion equation, multi-material flows, radiation hydrodynamics, plasma physics.

## 1 Introduction

### 1.1 Three temperature multi-material hydrodynamics

In applications such as Inertial Confinement Fusion [6] or astrophysics, the materials under scrutiny are usually plasmas. The behavior of strongly ionized plasmas is characterized by different thermalization time scales. Ions and electrons individually reach thermal equilibrium on characteristic times much shorter than those necessary for the mixture thermalization. If the hydrodynamic time scale falls between the two, a two-temperature description of the plasma is necessary; ions and electrons each have their own temperature but both temperatures need not be equal. Likewise, in the presence of

*Corresponding author. *Email address:* `sebastien.guisset@cea.fr` (S. Guisset)

 

a strong radiation field, photons need their own description which is here given by the grey diffusion approximation. Such an approximation is relevant in the optically thick limit if radiation thermalization is assumed [35]. The resulting three different temperatures are coupled through collisions between ions and electrons and between electrons and photons. These couplings can be arbitrarily stiff and the single-temperature Euler equations are recovered in the case of instantaneous relaxation. Besides, radiation transport accounts for the propagation of photons throughout the domain and can also display a stiff behavior. Diffusion on the ionic and electronic energies exists as well but are here neglected.

The physical description can be supplemented with an additional multi-material layer. Multi-material aspects are essential to properly describe complex mixtures with contrasted physical characteristics (e.g. mixtures of gases and solids). The most common approach to derive multi-material equations is that of conditional averaging procedures [18,25,42]. It produces averaged quantities describing the behavior of the flow, as well as additional correlation terms which encapsulate the remaining details. These correlation terms are often neglected as a first approximation as they are deemed minor, at least outside of shocks. If this approach has proven its efficiency in describing single-temperature multi-material flows, its application to radiation transport is not trivial. Indeed, averaged fluxes only express radiation transport separately within each material while the associated correlation term deals with the coupling between different materials. While radiation transport in between materials is essential for weakly opaque mixtures of materials, its expression remains unclear and heavily mixture-dependant. Alternatively, if it is neglected as a first approximation, then different materials are no longer coupled through temperatures, thus leading to questionable results.

## 1.2 Numerical strategy

### 1.2.1 Multi-material radiation transport or diffusion

The discretization of the multi-material radiation transport consists in one of the main contribution of this work. As explained above, its expression at the continuous level is a difficult task. Still, its discretization is possible and different strategies exist in the literature. Interface reconstruction techniques [14,21,37] estimate the interface between materials inside mixed cells. Mixed cells are then separated into pure cells and the diffusion operator is discretized with any single material strategy. At their best, these techniques allow for a very accurate description of the mixture. However, complex topology of the flow requires ad hoc strategies [22] and interface reconstruction fails at describing dispersed phases. The treatment of three or more materials is usually not invariant under permutation of materials and depends on an arbitrary order [28]. Finally, the computational cost, especially in three dimensions, can be significant. Alternatively, homogenization methods [13] assume that mixture of different materials act as a single equivalent material. Such methods are inexpensive but are usually not considered reliable [13,27]. Apart from obvious accuracy issues on the fluxes, homogenization methods are built on

the assumption that all materials share the same temperature inside a given cell. Such hypotheses is not relevant for mixtures of materials with contrasted opacity or for applications where relaxation of temperatures cannot be considered instantaneous.

Here is presented the so-called discrete equation method (DEM) based on the ideas independently developed in [2,7,8] and latter used in numerous works including but not limited to [3, 38]. Instead of being dealt with as a local source term and approximated through interface reconstruction or instantaneous equalization, diffusion between materials takes place at each face, just like diffusion of a single material. This effectively bypasses the averaging procedure. The method remains both conceptually and computationally simple while test cases establish significant accuracy improvements over homogenization methods.

### 1.2.2 Multi-material hydrodynamics

The numerical strategy for the hydrodynamic part is based on the single material, single temperature GLACE/EUCCLHYD scheme [5,32]. The scheme is Lagrangian and can be integrated into an arbitrary-Lagrange-Euler (ALE) setting [20,24]. It will here be coupled with an alternate direction (AD) procedure [19,41], chosen for both its performance and simplicity.

Generally speaking, two main difficulties arise when starting from a single temperature and single material scheme and extending it to a three-temperature multi-material one. First, an evolution equation must be added for the material volumes. Here, the equal strain assumption is made and consists in saying that volume fractions stay constant during the Lagrangian phase [4]. This closure is chosen for simplicity although it may become irrelevant for mixture of materials with contrasted equations of state [23,33] (e.g. air and water). Second, first order models with several temperatures or several materials (and a fortiori with both) are not sufficient to characterize shocks. Indeed, only partial jump relationships (on individual masses, total momentum, total energy) exist and shocks are eventually small-scale dependant. The detail of the entropy production (which summarizes the contribution of the aforementioned correlation terms) is then necessary to fully describe shocks both at the continuous and at the discrete level.

### 1.2.3 Time integration of diffusion and relaxation processes

A three-temperature model allows the description of systems which are not at thermal equilibrium. Although diffusion and relaxation processes are not instantaneous, they are usually stiff and require an implicit time integration in order to keep decent time steps. Because of the non-linearity, iterative methods are usually considered. However, enforcing positivity of temperatures both at convergence and during the different iterations is not trivial and failing to do so can abruptly stop the computation.

The method considered here is a multi-material extension of [10]. The hydrodynamics, the radiation transport and the source terms are all treated at the same time without any splitting. As pointed out in [9], doing so allows to better capture the coupling between the different terms in radiation shocks where temperatures and densities experi-

ence large variations over few numerical cells. Contrary to some approaches in the literature [9,39], radiation transport and source terms are here fully implicited (i.e. the implicitation concerns the global terms and not only the temperatures or energies). This choice arguably offers better robustness with respect to sudden changes in the constitutive laws of collision frequencies, opacities and diffusion coefficients; the effects of similar changes on the pressure were studied in [23] where they were referred to as "stiff stiffness". The system resulting from the full time implicitation is however all the more non-linear and harder to solve numerically. The present strategy is based on convex combinations and ensures that temperatures all stay positive during the iterative procedure.

The article is organized as follows. In Section 2, the three-temperature multi-material equations are presented. In Section 3, the multi-material heat equation is discretized thanks to the DEM. This equation and strategy serve as a prototype for dealing with the radiation transport in the three-temperature multi-material equations. In Section 4, the numerical approximation of the complete system of equations is addressed. Robustness in the presence of stiffness is achieved through a specific temporal discretization based on convex combinations.

## 2 Three-temperature multi-material equations

### 2.1 Three-temperature single-material equations

The notations are standard with $\rho$ the density, $\mathbf{u}$ the velocity, $e_i$ and $e_e$ the specific ionic and electronic internal energies, and $e_r$ the volumetric radiation energy. Additionally, ions and electrons are described with an equation of state $e_\theta(1/\rho, s_\theta)$, $\theta \in \{i,e\}$ where $s_\theta$ is the species entropy. Pressures and temperatures are then defined by Gibbs relationship

$$\mathrm{d}e_\theta = -p_\theta \mathrm{d}\left(\frac{1}{\rho}\right) + T_\theta \mathrm{d}s_\theta. \tag{2.1}$$

Positivity of temperature and density allows to express all quantities as functions of the density $\rho$ and the internal energy $e_\theta$ [34]. Likewise, photons have their own pressure, temperature and entropy, defined by

$$p_r = \frac{e_r}{3}, \tag{2.2a}$$

$$e_r = aT_r^4, \tag{2.2b}$$

$$\mathrm{d}\left(\frac{e_r}{\rho}\right) = -p_r \mathrm{d}\left(\frac{1}{\rho}\right) + T_r \mathrm{d}s_r, \tag{2.2c}$$

where $a$ is the radiation constant. The three-temperature equations [10] are here written in the Lagrangian formalism which factorizes transport into time derivatives. It lays the

foundations for the "Lagrange + Remap" approach used in Section 4,

$$\rho\frac{\mathrm{d}}{\mathrm{d}t}\left(\frac{1}{\rho}\right)=\nabla\cdot\mathbf{u}, \tag{2.3a}$$

$$\rho\frac{\mathrm{d}}{\mathrm{d}t}\mathbf{u}=-\nabla p, \tag{2.3b}$$

$$\rho\frac{\mathrm{d}}{\mathrm{d}t}e_i=-\rho p_i\frac{\mathrm{d}}{\mathrm{d}t}\left(\frac{1}{\rho}\right)+c\kappa(T_e-T_i), \tag{2.3c}$$

$$\rho\frac{\mathrm{d}}{\mathrm{d}t}e_e=-\rho p_e\frac{\mathrm{d}}{\mathrm{d}t}\left(\frac{1}{\rho}\right)+c\kappa(T_i-T_e)+c\sigma_P\left(aT_r^4-aT_e^4\right), \tag{2.3d}$$

$$\rho\frac{\mathrm{d}}{\mathrm{d}t}\left(\frac{e_r}{\rho}\right)=-\rho p_r\frac{\mathrm{d}}{\mathrm{d}t}\left(\frac{1}{\rho}\right)-\nabla\cdot\mathbf{F}_r+c\sigma_P\left(aT_e^4-aT_r^4\right). \tag{2.3e}$$

The different temperatures are coupled through relaxation terms driving the system toward local thermal equilibrium $T_e=T_i=T_r$. The coupling between ions and electrons is given by a relaxation coefficient $\kappa$, while the coupling between electrons and photons is given by Planck's opacity $\sigma_P$. Both coefficients are functions of the different temperatures. $c$ is the speed of light. The radiation flux $\mathbf{F}_r$ couples spatially photon temperatures from one place to another, thus driving the system towards an homogenization state $\nabla T_r=0$. It is here expressed accordingly to the Rosseland diffusion approximation [35]

$$\mathbf{F}_r=-\frac{c}{3\sigma_R}\nabla e_r, \tag{2.4}$$

where the Rosseland opacity $\sigma_R$ is a function of the electronic temperature $T_e$. Physically, ionic and electronic transport should also be considered but they are usually weaker and here completely neglected. Thanks to these terms (namely relaxation terms and radiation transport), thermal equilibrium is not instantaneous but may still be stiff. Eqs. (2.3c)-(2.3e) are deliberately written in a consistent manner with (2.1), (2.2c) so that it becomes obvious that the individual entropy productions are given by the relaxation terms and the diffusion

$$\rho T_i\frac{\mathrm{d}}{\mathrm{d}t}s_i=c\kappa(T_e-T_i), \tag{2.5a}$$

$$\rho T_e\frac{\mathrm{d}}{\mathrm{d}t}s_e=c\kappa(T_i-T_e)+c\sigma_P\left(aT_r^4-aT_e^4\right), \tag{2.5b}$$

$$\rho T_r\frac{\mathrm{d}}{\mathrm{d}t}s_r=\nabla\cdot\left(\frac{c}{3\sigma_R}\nabla e_r\right)+c\sigma_P\left(aT_e^4-aT_r^4\right). \tag{2.5c}$$

The evolution of the total entropy $s=s_i+s_e+s_r$ thus reads

$$\begin{aligned}\rho\frac{\mathrm{d}}{\mathrm{d}t}s&=\frac{1}{T_r}\nabla\cdot\left(\frac{c}{3\sigma_R}\nabla e_r\right)+c\kappa(T_i-T_e)\left(\frac{1}{T_e}-\frac{1}{T_i}\right)+c\sigma_P\left(aT_e^4-aT_r^4\right)\left(\frac{1}{T_r}-\frac{1}{T_e}\right)\\&=-\nabla\cdot\left(\frac{\mathbf{F}_r}{T_r}\right)+\frac{4acT_r}{3\sigma_R}\|\nabla T_r\|^2+c\kappa\frac{(T_i-T_e)^2}{T_iT_e}+ca\sigma_P\frac{(T_e-T_r)\left(T_e^4-T_r^4\right)}{T_eT_r}.\end{aligned} \tag{2.6}$$

Every term in the right-hand side is either positive or a flux thus complying with the second principle of thermodynamics. Finally, the total pressure is $p = p_i + p_e + p_r$ and conservation of total energy is then given by

$$\rho \frac{\mathrm{d}}{\mathrm{d}t}\left(\frac{\|\mathbf{u}\|^2}{2} + e_i + e_e + \frac{e_r}{\rho}\right) = -\nabla\cdot(p\mathbf{u} + \mathbf{F}_r). \tag{2.7}$$

## 2.2 Multi-material aspects

An arbitrary number of material is now considered. The general methodology to derive multi-material equations is based on a conditional averaging procedure introduced in [25] and summarized in [42] for non-miscible materials and in [23, Appendix B] for general mixtures. The averaging may be spatial, temporal or statistical. In all cases, averaged quantities and averaged fluxes are defined for all materials but some residuals (or correlation terms) remain unspecified and are often neglected as a first approximation. Additionally, the model can be subsequently simplified if materials are assumed to be at local velocity, pressure or temperature equilibrium. Such hypothesis depend on the characteristic times of observation. Here, it is assumed that thermal equilibrium is not reached while pressure and velocity equilibrium are sensible approximations [26]. Eventually, the three-temperature single-velocity multi-material equations read

$$\alpha^k \rho^k \frac{\mathrm{d}}{\mathrm{d}t}\left(\frac{1}{\alpha^k \rho^k}\right) = \nabla\cdot\mathbf{u}, \tag{2.8a}$$

$$\rho \frac{\mathrm{d}}{\mathrm{d}t}\mathbf{u} = -\nabla p, \tag{2.8b}$$

$$\alpha^k \rho^k \frac{\mathrm{d}}{\mathrm{d}t} e_i^k = -\alpha^k \rho^k p_i^k \frac{\mathrm{d}}{\mathrm{d}t}\left(\frac{1}{\rho^k}\right) + \alpha^k c\kappa^k \left(T_e^k - T_i^k\right), \tag{2.8c}$$

$$\alpha^k \rho^k \frac{\mathrm{d}}{\mathrm{d}t} e_e^k = -\alpha^k \rho^k p_e^k \frac{\mathrm{d}}{\mathrm{d}t}\left(\frac{1}{\rho^k}\right) + \alpha^k c\kappa^k \left(T_i^k - T_e^k\right) + \alpha^k c\sigma_P^k \left(e_r^k - a\left(T_e^k\right)^4\right), \tag{2.8d}$$

$$\alpha^k \rho^k \frac{\mathrm{d}}{\mathrm{d}t}\left(\frac{e_r^k}{\rho^k}\right) = -\alpha^k \rho^k p_r^k \frac{\mathrm{d}}{\mathrm{d}t}\left(\frac{1}{\rho^k}\right) - \nabla\cdot\left(\alpha^k \mathbf{F}_r^k\right) + \alpha^k c\sigma_P^k \left(a\left(T_e^k\right)^4 - E_r^k\right). \tag{2.8e}$$

The indices $k$ refer to the averaged quantities related to material $k$. $\alpha^k$ is the volume fraction of material $k$ while $\rho$ is the total density

$$\rho = \sum_k \alpha^k \rho^k. \tag{2.9}$$

Although the averaging process alleviates the treatment of interfaces, certain details of the flow are lost and, as such, model (2.8) is underdetermined. Closures need to be provided.

- The first one concerns the evolution of either densities, volume fractions or pressures and ensures that the number of equations equals the number of unknowns.

In keeping with the previous considerations on pressure equilibrium, a sound closure would consists in the equality of material pressures. The numerical treatment of pressure equalization is challenging in the context of a three-temperature multi-material model with stiff source terms. It is here left out in favor of the simpler equal strain assumption

$$\alpha^k \rho^k \frac{\mathrm{d}}{\mathrm{d}t}\left(\frac{1}{\rho^k}\right) = \alpha^k \nabla \cdot \mathbf{u} \quad \Longleftrightarrow \quad \frac{\mathrm{d}}{\mathrm{d}t}\alpha^k = 0. \tag{2.10}$$

This approximation is physically questionable when dealing with highly contrasted mixtures. A discussion on these two closures is done in [33]. The total pressure then needs to be

$$p = \sum_k \alpha^k \left(p_i^k + p_e^k + p_r^k\right), \tag{2.11}$$

so as to ensure total energy conservation. The resulting first order system (without diffusion or source terms) is hyperbolic with eigenvalues $-c+u, u, c+u$ where $c$ is the speed of sound of the mixture

$$\rho c^2 = \sum_k \alpha^k \rho^k \left( \left.\frac{\partial p_i^k}{\partial \rho}\right|_{s_i^k} + \left.\frac{\partial p_e^k}{\partial \rho}\right|_{s_e^k} + \left.\frac{\partial p_s^k}{\partial \rho}\right|_{s_s^k} \right). \tag{2.12}$$

- Even with the right amount of equations, the behavior of the mixture is still not defined inside shocks. Indeed, multi-temperature multi-material shocks are small-scale dependent which means that no complete jump relationships can be written without knowing the details of what is happening inside the shock [26]. Mathematically, this failure comes from the presence of non-conservative products which prevents any canonical weak formulation from being written [12]. In practice, entropy production on each material and on each species (i.e. ions, electrons and photons) encapsulates the details of the small-scale effects and entirely determines the shock.

- The averaged radiation flux $\nabla \cdot (\alpha^k \mathbf{F}_r^k)$ only describes parallel diffusion for each material separately. The physically necessary coupling between materials is actually hidden in the previously neglected correlation terms. Such correlation terms could be modelled as local source terms coupling temperatures of different materials but their expression would be heavily mixture dependant. One of the main contribution of the present work concerns the discretization of the multi-material radiation transport and is discussed in Section 3.

Concerning the entropy production of the multi-material model, an inequality similar to (2.6) can be derived. However, the expression of the radiation transport in (2.8e) will not be discretized as it is. It will be seen that the chosen approach also leads to an entropy inequality at the discrete level, as well as total energy conservation.

# 3 Numerical strategies for the multi-material heat equation

In this section, the full three-temperature picture is reduced in order to focus only on the multi-material aspects of the radiation transport. The prototype is the so-called heat equation

$$\partial_t T = \nabla \cdot (\kappa \nabla T). \tag{3.1}$$

The thermal conductivity $\kappa$ is assumed to depend on the temperature $T$ and the space coordinate $x$. The space dependence reflects the multi-material aspects as $\kappa$ may experience discontinuities in the vicinity of the interfaces between different materials. In the following, two methods (namely the homogenization method and the DEM) are presented for the numerical approximation of (3.1) in the context of mixed cells, i.e. cells containing more than one material and thus as many temperatures and thermal conductivities.

## 3.1 Homogenization methods: Principles and limits

In the case of the so-called homogenization methods [13], mixed cells are assumed to contain a fictive single material. It is described by only one temperature $\overline{T}_c$ and one thermal conductivity $\overline{\kappa}_c$ which is an average of the thermal conductivities of the real materials, weighted by their volume fractions,

$$\overline{\kappa}_c = \phi^{-1}\left(\sum_k \alpha_c^k \phi\left(\kappa_c^k\right)\right). \tag{3.2}$$

The mean is arithmetic for $\phi(x) = x$ and harmonic for $\phi(x) = 1/x$. Other choices are possible as long as $\phi$ is strictly monotonic and positive, but they will not be considered in the following. The flux between cells $c$ and $d$ is then written

$$\overline{\mathrm{F}}_{cd} = \overline{\kappa}_c \frac{\overline{T}_{cd} - \overline{T}_c}{h_{cd}} S_{cd}, \tag{3.3}$$

where $\overline{T}_{cd}$ is the temperature at the interface between cells $c$ and $d$. $h_{cd}$ and $S_{cd}$ are respectively the distance between the center of $\omega_c$ and the interface, and the surface of the interface.

**Remark 3.1.** Continuity of the temperature at the interface implies $T_{cd} = T_{dc}$. Likewise, geometrical considerations simply leads to $S_{cd} = S_{dc}$. Finally, $h_{cd}$ obeys to no particular symmetry.

Homogenization methods may induce accuracy issues. Indeed, allowing only one temperature inside each cell is a strong approximation which does not account for mixtures with highly contrasted thermal conductivity [27] (or opacity for radiation transport). Because diffusion has a regularizing effect, temperatures are theoretically continuous across interfaces between different materials. However, steep temperature gradients

may exist so that temperatures cannot be numerically considered constant inside cells close to these interfaces.

These accuracy issues have cascading effects in the context of three-temperature hydrodynamics. For a given material, electronic, ionic and photon temperatures are coupled through relaxation terms. These couplings are stiff and may occur on characteristic times smaller than those of diffusion for opaque materials. Equality of photon temperatures does not comply with this hierarchy and indirectly produces a non-physical coupling between ionic and electronic temperatures of different materials. This is critical when considering chemical or nuclear reactions depending on temperature thresholds. They may be spuriously triggered or turned off leading to physically questionable results.

## 3.2 DEM-based discretization

The present strategy follows the idea in [2,7,8]. Instead of discretizing the averaged equations, the single material equations are first implicitly discretized before being averaged at the discrete level. Fluxes between materials now take place at the interface between cells instead of only being dealt with as local source terms. The method is here described as implicitly resulting from an interface reconstruction where the different geometrical quantities are estimated inexpensively without sacrificing too much accuracy. An interface reconstruction implies that the averaging procedure is spatial as it is explained in [8] with the so-called stratified flow model. Probabilistic averaging can also be taken as it is done in [2]. All averaging share the same algebraic properties so that the different approaches result in formally equivalent schemes.

### 3.2.1 Generic formulation

Considering a mixed cell $c$ and assuming that the position of each material is known (with an interface reconstruction technique for example), the heat equation may be integrated

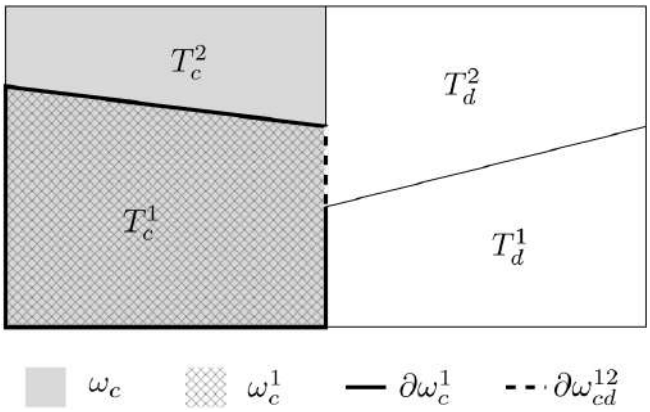


Figure 1: Example of two adjacent mixed cells and the corresponding notations for the geometry. The volume $\omega_c$ contains the sub-volume $\omega_c^1$. Likewise, the surface $\partial\omega_{cd}^{12}$ is includes inside the surface $\partial_c^1$.

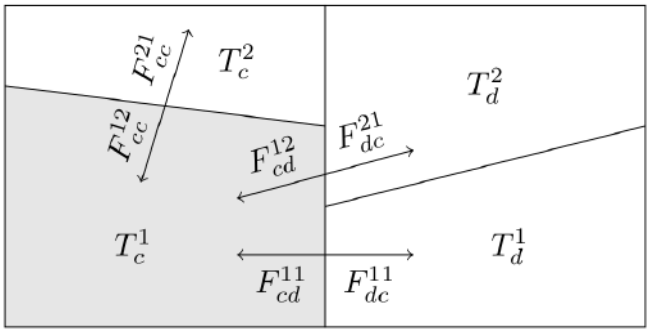


Figure 2: Same configuration as in Fig. 1 with the fluxes.

on each material sub-volume $\omega_c^k$ leading to

$$\int_{\omega_c^k} \partial_t T dv = \int_{\partial\omega_c^k} (\kappa \nabla T) \cdot \mathbf{n} ds. \tag{3.4}$$

Then dividing the surface $\partial\omega_c^k$ into sub-surfaces $\partial\omega_{cd}^{kl}$ where material $k$ of cell $c$ is in contact with material $l$ of cell $d$ (it is not excluded that $c=d$), Eq. (3.4) becomes

$$\int_{\omega_c^k} \partial_t T dv = \sum_{l,d} \int_{\partial\omega_{cd}^{kl}} (\kappa \nabla T) \cdot \mathbf{n} ds = \sum_{l,d} \mathrm{F}_{cd}^{kl}. \tag{3.5}$$

The sum may be taken over all materials and over all cells by arbitrarily defining $\mathrm{F}_{cd}^{kl}=0$ when both materials or cells are not in contact. A generic expression of these fluxes is the following:

$$\mathrm{F}_{cd}^{kl} = \kappa_c^k \frac{T_{cd}^{kl} - T_c^k}{h_{cd}^{kl}} S_{cd}^{kl}, \tag{3.6}$$

where the notations are similar to that of the homogenization case, except they now depend on a pair of materials.

- $h_{cd}^{kl}$ is the distance between the center of the sub-cell $\omega_c^k$ and the interface between material $k$ of cell $c$ and material $l$ of cell $d$.
- $T_{cd}^{kl}$ is the temperature at the interface between the two materials.
- $S_{cd}^{kl}$ is the area of the interface between the two materials. It is set as a portion $\delta_{cd}^{kl}$ of the entire surface $S_{cd}$ between the two cells $S_{cd}^{kl} = \delta_{cd}^{kl} S_{cd}$.

**Remark 3.2.** Symmetries detailed in Remark 3.1 are still valid (namely $T_{cd}^{kl} = T_{dc}^{lk}$ and $S_{cd}^{kl} = S_{dc}^{lk}$). They hold because both terms involve the same pair of materials. On the other hand, there is no reason for $T_{cd}^{kl}$ to be equal to $T_{cd}^{lk}$ or $T_{dc}^{kl}$ (and likewise for $S$).

Here, no information concerning the geometry of the mixed cell is assumed. In particular, the position of each material inside the cell and their surface of contact at each interfaces with neighbor cells is not known. Nevertheless, an approximation of $\mathrm{F}_{cd}^{kl}$ is still possible. Fluxes between different cells (i.e. $c \neq d$) are treated similarly to [2, 7, 8]. The method is described in the Section 3.2.2. Internal fluxes (i.e. $c = d$) are discussed in Section 3.2.3.

### 3.2.2 Computations of the geometry

The distances $h_{cd}^{kl}$ are taken as the distance between the center of the cell $\omega_c$ and the face between cells $c$ and $d$. It does not depend on materials $k$ and $l$ and consists in a neutral standing point as, again, the location of each material inside the cell remains unknown.

Regarding proportions $\delta_{cd}^{kl}$, the strategy retained is that of [2,7,8]. $\delta_{cd}^{k}$ denotes the total surface fraction of material $k$ at the interface between cells $c$ and $d$. The surface fraction may be discontinuous so that $\delta_{cd}^{k} \neq \delta_{dc}^{k}$. Parameters $\delta_{cd}^{kl}$ are then constrained by

$$\sum_{l} \delta_{cd}^{kl} = \delta_{cd}^{k}, \quad \forall k, \tag{3.7a}$$

$$\sum_{k} \delta_{cd}^{kl} = \delta_{dc}^{l}, \quad \forall l. \tag{3.7b}$$

Without any information on the location of each material inside the cell, these surface fractions can be reasonably approximated by the volume fraction of the associated cell $\delta_{cd}^{k} = \alpha_c^k$. For the sake of readability, the following analysis of system (3.7) is restricted to the case of two materials 1 and 2. The case of an arbitrary number of materials is discussed in Appendix A

$$\delta_{cd}^{11} + \delta_{cd}^{12} = \alpha_c^1, \tag{3.8a}$$

$$\delta_{cd}^{21} + \delta_{cd}^{22} = \alpha_c^2, \tag{3.8b}$$

$$\delta_{cd}^{11} + \delta_{cd}^{21} = \alpha_d^1, \tag{3.8c}$$

$$\delta_{cd}^{12} + \delta_{cd}^{22} = \alpha_d^2. \tag{3.8d}$$

System (3.8) consists in four equations and four unknowns. It is not invertible as the last equation is redundant and can be deduced from the other 3. A general solution is then of the form

$$\delta_{cd}^{11} = \alpha_c^1 \alpha_d^1 + \lambda, \tag{3.9a}$$

$$\delta_{cd}^{12} = \alpha_c^1 \alpha_d^2 - \lambda, \tag{3.9b}$$

$$\delta_{cd}^{21} = \alpha_c^2 \alpha_d^1 - \lambda, \tag{3.9c}$$

$$\delta_{cd}^{22} = \alpha_c^2 \alpha_d^2 + \lambda, \tag{3.9d}$$

where $\lambda$ is a real-valued degree of freedom. Because surface fractions need to stay in $[0,1]$, $\lambda$ is bounded

$$-\min\left(\alpha_c^1 \alpha_d^1, \alpha_c^2 \alpha_d^2\right) \leq \lambda \leq \min\left(\alpha_c^1 \alpha_d^2, \alpha_c^2 \alpha_d^1\right). \tag{3.10}$$

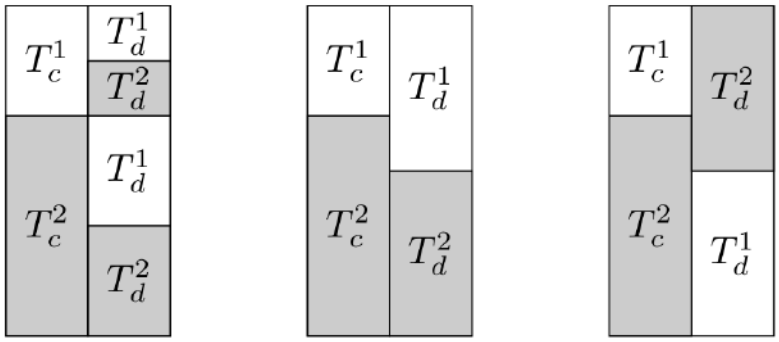


Figure 3: Examples of the $\lambda_0$ (left), $\lambda_{\max}$ (center) and $\lambda_{\min}$ (right) cases for given surface fractions. On each scheme, the center line corresponds to the interface. As an example, the proportion $\delta_{cd}^{12}$ is the ratio of the surface shared by rectangles $T_c^1$ and $T_d^2$ on the total surface of the interface (i.e. $1/6$ for $\lambda_0$, $0$ for $\lambda_{\max}$ and $1/3$ for $\lambda_{\min}$).

In this continuum, three cases (displayed in Fig. 3) are retained for the rest of the work:

- $\lambda = 0$ which adds no a priori with the way materials interact with each other. This choice was already explored in [7]. It will be referred to as $\lambda_0$ in the following.
- $\lambda = \min(\alpha_c^1\alpha_d^2, \alpha_c^2\alpha_d^1)$ for which interactions between the same material are preferred. This corresponds to the stratified flow model detailed in [8]. In [2], it is associated to separate phase flows. It will be referred to as $\lambda_{\max}$.
- $\lambda = -\min(\alpha_c^1\alpha_d^1, \alpha_c^2\alpha_d^2)$ which maximizes the surface between pairs of different materials. In [2], it is associated to dispersed flows. It will be referred to as $\lambda_{\min}$.

**Remark 3.3.** Estimations of distances $h_{cd}^{kl}$ or surface fractions $\delta_{cd}^k$ can be honed using additional information provided by estimations of volume fraction gradients. This is the usual starting point of an interface reconstruction [37] although it is possible to extract the information of interest while bypassing the bulk of the procedure. Hence, greater accuracy could be achieved without a significant increase in computation time. Here, (limited) linear reconstruction of coefficients $\delta_{cd}^k$ will be considered.

### 3.2.3 Internal flux

Physically, an internal flux should be considered inside mixed cell in order to drive materials toward temperature equilibrium. Internal fluxes are usually computed through interface reconstructions. Still, this formulation is not relevant for dispersed phases and does not extend easily to more than two materials and three dimensions. These issues were already discussed earlier and were the reason why discretizing the averaged model was first excluded in favor of the DEM. In the previous installments of the DEM ideas, no internal flux is considered. Such a term is not necessary as materials inside a given cell still interact indirectly as they are coupled through materials of neighbor cells. Caution still need to be exercised in two singular cases:

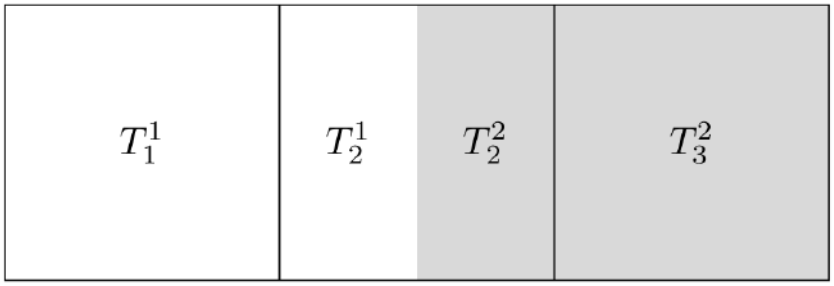


Figure 4: With an anti-diffusive high order technique, the estimation of the volume fraction $\delta_{23}^2$ can reach 1 so that the flux between cell 2 and cell 3 concerns material 2. Symmetrically, the volume fraction $\delta_{21}^1$ is also 1 so that the flux between cell 1 and cell 2 concerns material 1. Then, both materials do not interact at all with each other.

- If $\lambda_{\max}$ is chosen and volume fraction is constant across the entire domain, then the different materials no longer interact and diffusion occurs in parallel inside each material.
- If surface fractions are estimated with a strongly anti-diffusive limiter (as explained in Remark 3.3), they can be 0 or 1 even if the cell volume fraction is not (see Fig. 4). In this case, all choices of $\lambda$ are equivalent and materials do not interact with each other.

Even if the choice $\lambda_{\max}$, combined with high order reconstruction techniques, may seem desirable at first for accurately capturing dispersed phases, they are not compatible with the omission of an internal flux.

## 3.3 Conservation and practical computations of the fluxes

Up until now, every fluxes have been expressed in terms of surface temperatures which are yet to be specified. Conservation of the scheme heavily constrains surface temperatures although some leeway exists for the DEM.

### 3.3.1 The case of homogenization methods

For homogenization methods, only one temperature is considered for each cell and each face. Continuity of the flux holds at the interface between two materials

$$\overline{\mathrm{F}}_{cd} = -\overline{\mathrm{F}}_{dc}. \tag{3.11}$$

Eq. (3.11) also immediately guarantees that the scheme is conservative. Solving for $\overline{T}_{cd} = \overline{T}_{dc}$ in Eq. (3.11) eventually yields

$$\overline{\mathrm{F}}_{cd} = \overline{\kappa}_{cd} \frac{\overline{T}_d - \overline{T}_c}{h_{cd} + h_{dc}} S_{cd}, \tag{3.12a}$$

$$\overline{T}_{cd}=\left(\frac{\overline{\kappa}_c}{h_{cd}}\overline{T}_c+\frac{\overline{\kappa}_d}{h_{dc}}\overline{T}_d\right)\left(\frac{\overline{\kappa}_c}{h_{cd}}+\frac{\overline{\kappa}_d}{h_{dc}}\right)^{-1}, \tag{3.12b}$$

$$\overline{\kappa}_{cd}=(h_{cd}+h_{dc})\left(\frac{h_{cd}}{\overline{\kappa_c}}+\frac{h_{dc}}{\overline{\kappa_d}}\right)^{-1}. \tag{3.12c}$$

### 3.3.2 The case of the discrete equation method

In the case of DEM, two approaches may be distinguished. First, as in [27], only one temperature is allowed on each face. Consequently, only one equation is needed to fully define the scheme. A global conservation is chosen

$$\sum_k \mathrm{F}_{cd}^{kl}=-\sum_l \mathrm{F}_{dc}^{lk}. \tag{3.13}$$

Alternatively, one may consider as many temperatures as there are couples of materials interacting at the face. Because of these new degrees of freedom, conservation for individual fluxes is possible

$$\mathrm{F}_{cd}^{kl}=-\mathrm{F}_{dc}^{lk}. \tag{3.14}$$

It is the latter choice which is retained. Indeed, having allowed more than one temperature inside the cell, it seems counterproductive to then only allow one temperature on each face. Just as for (3.12), (3.14) gives

$$\mathrm{F}_{cd}^{kl}=\kappa_{cd}^{kl}\frac{T_d^l-T_c^k}{h_{cd}^{kl}+h_{dc}^{lk}}S_{cd}^{kl}, \tag{3.15a}$$

$$T_{cd}^{kl}=\left(\frac{\kappa_c^k}{h_{cd}^{kl}}T_c^k+\frac{\kappa_d^l}{h_{dc}^{lk}}T_d^l\right)\left(\frac{\kappa_c^k}{h_{cd}^{kl}}+\frac{\kappa_d^l}{h_{dc}^{lk}}\right)^{-1}, \tag{3.15b}$$

$$\kappa_{cd}^{kl}=\left(h_{cd}^{kl}+h_{dc}^{lk}\right)\left(\frac{h_{cd}^{kl}}{\kappa_c^k}+\frac{h_{dc}^{lk}}{\kappa_d^l}\right)^{-1}. \tag{3.15c}$$

**Remark 3.4.** Fluxes may be written in the generic form

$$F_{cd}^{kl}=A_{cd}^{kl}\left(T_d^l-T_c^k\right) \tag{3.16}$$

with $A_{cd}^{kl}=A_{dc}^{lk}\geq 0$. This factorized form will be used for the three-temperature multimaterial scheme for best readability.

## 3.4 Numerical results and comparison of the two methods

The different test cases aim at comparing the performances of the different methods. The numerical error depends both on the number of cells and the relative position of the mesh with respect to the physical interfaces. Increasing the mesh size without changing its relative position from the interfaces amounts to measure the order of convergence of

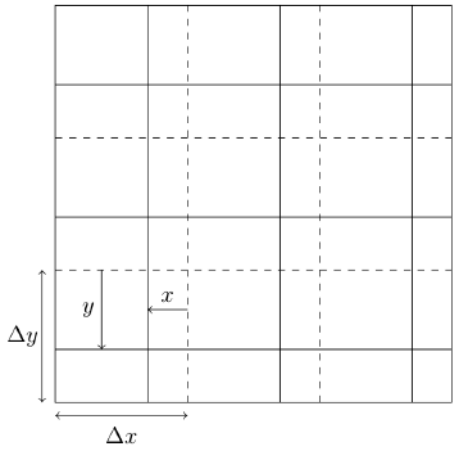


Figure 5: Initial mesh (dashed lines) and shifted mesh (full lines). The shift is parameterized by the lengths $x$ and $y$. The relative $x$-shift is given by $x/\Delta x \in [0,1]$ (and likewise for $y$).

the different methods. The order of convergence is an important feature of numerical schemes but it is somewhat an orthogonal issue to what is investigated in this work. Besides, no significant difference in the order of convergence is expected; in particular, if the mesh is perfectly aligned with the interfaces, all methods are equivalent and the order will exactly be the same.

Here, performance is measured in terms of robustness with respect to changes of volume fraction. More precisely, the mesh size is fixed and the focus is put on how accuracy deteriorate when the mesh undergoes arbitrary displacements. For a cartesian mesh, the displacement is here given as a function of two parameters: the $x$-shift and the $y$-shift as depicted in Fig. 5. The $x$-shift is the relative displacement parallel to the $x$-axis. Two values of $x$-shift which are equal modulo 1 give the same mesh so only values in $[0,1]$ are considered. In particular, the values 0 and 1 induce no change on the mesh. Same goes for the $y$-shift.

In all test cases, the different methods are denoted with their own specific key. For homogenization methods, it is respectively A for the arithmetic mean and H for the harmonic mean. The discrete equation method's key is identified with the letter L and is then given in order by: the choice of $\lambda$ (0, min or max), the reconstruction of volume fractions (1 constant and 2 for linear) and the use of internal flux (F if none is used and T otherwise). For instance Lmin2F stands for the DEM with the choice $\lambda_{\min}$, linear reconstruction of volume fractions and no internal flux. Finally, time integration is implicit and not subject to any stability restriction on the time step.

### 3.4.1 Layered wall

The first test case consists in a wall with multiple layers of two distinct materials. The domain of the wall $[0,1]\times[0,0.1]$ is divided into 8 equal parts along the $x$-axis as shown in Fig. 6. The first material of thermal conductivity $\kappa^1 = 1$ occupies the first, third, fifth and

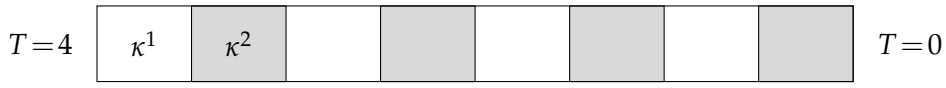


Figure 6: Layered wall configuration.

seventh parts; the second material of thermal conductivity $\kappa^2=10^{-2}$ occupies the rest of the domain. Dirichlet boundary conditions are set with $T=4$ on the left border, and $T=0$ on the right. Fluxes are set to zero along the top and bottom borders so that the test case is essentially one-dimensional. The layout of the problem is summarized in Fig. 6.

The problem is discretized on $N_x\times 1$ meshes with $N_x=32$ and $N_x=160$. Because in both cases $N_x\equiv 0[8]$, the unperturbed mesh only consists of pure cells. A non zero $x$-shift produces mixed cells whose effect is analysed. Results at $t=5$ computed with times steps $\Delta t=1$ and various values of $x$-shift are compared with a reference solution. The reference is computed on a $12\,800\times 1$ mesh consisting of only pure cells.

Results are summarized in Fig. 7. Homogenization methods perform differently depending on the mean. Arithmetic mean gives the worst accuracy; the error skyrockets even for small displacements of the mesh. Harmonic mean fares well, even better than the DEM. It can actually be shown that, for this particular problem, it gives exact global stationary fluxes. As for the DEM, the value of $\lambda$ cannot be changed because there is no adjacent mixed cells. Only the linear reconstruction of volume fractions and the internal flux can be studied. The linear reconstruction seems to significantly improve the results, except for $x$-shifts close to 0.5. For small displacements (i.e. with an $x$-shift or volume fraction close to 0 or to 1), the linear reconstruction helps mitigate the presence of the material in minority. However, for balanced mixed cell, it seriously underestimates the

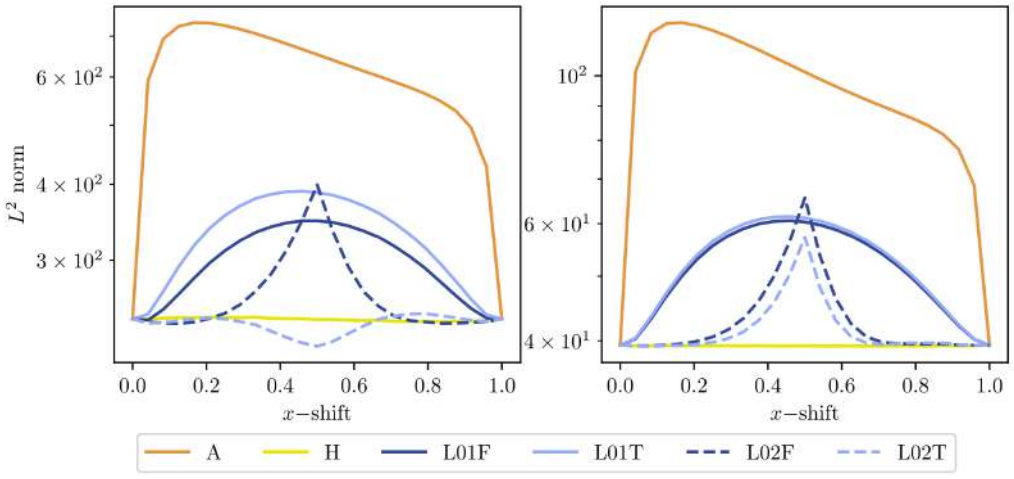


Figure 7: $L^2$ error as a function of the displacement of the mesh for the layered wall test case. Left: $32\times 1$ mesh. Right: $160\times 1$ mesh.

flux between the two materials (as explained in Remark 3.2.3). This is the reason why an additional internal flux decreases the error. However, its effect fades out for a greater number of cells. It becomes less relevant as the underlying solution is continuous and refining the mesh means that temperature inside mixed cell converge to one another.

### 3.4.2 Sandwich problem

While the previous test case was interested in fluxes orthogonal to the interface, the so-called sandwich problem [27] studies fluxes parallel to the interface. The domain $[0,0.5]\times[0,1]$ is shared between two materials as depicted in Fig. 9: The first one, with a thermal conductivity $\kappa_1=1$ occupies the zone $0.05\leq x\leq 0.45$; the rest of the domain contains a material of thermal conductivity $\kappa_2=0$. Temperature is set to $T=1$ at the bottom, and $T=0$ at the top. Fluxes are set to zero along the left and right borders. Because the exterior material does not conduct heat, the solution inside the interior material is essentially one-dimensional.

The problem is discretized on a $40\times80$ mesh and results are compared with a reference solution computed on a $500\times1000$ mesh. Once again, because the number of horizontal cell is a multiple of 10, the unperturbed meshes consist only of pure cells. The final time is $t=1$ with a time step of $\Delta t=0.1$.

Results are given in Fig. 8. Homogenized methods give similarly poor results: small displacements of the mesh induce strong errors for both arithmetic and harmonic means. The DEM gives substantially better results. Here, no internal flux is considered as the second material does not conduct heat. Linear reconstruction of volume fractions has almost no effect as it only concerns horizontal fluxes which are supposed to be zero as

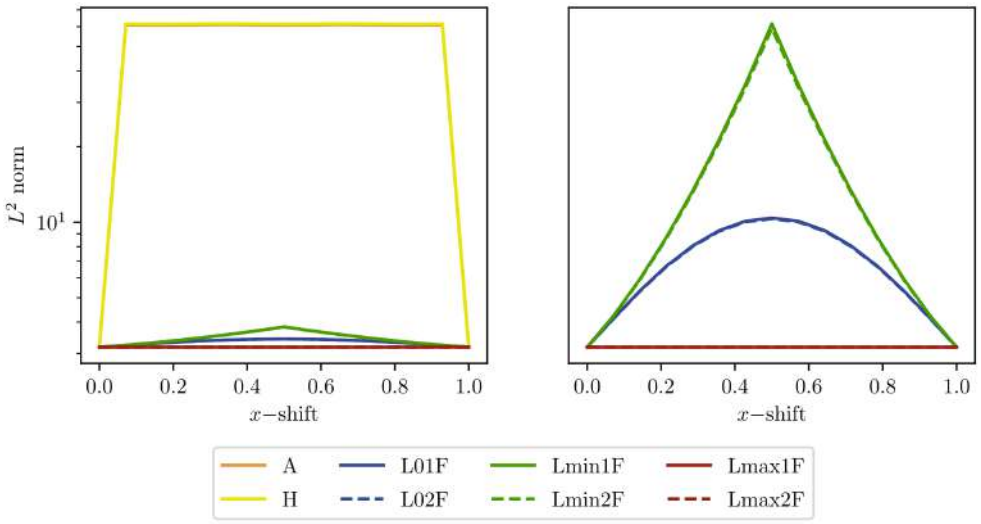


Figure 8: $L^2$ error as a function of the displacement of the mesh for the sandwich problem. Left: for all methods. Right: only for the DEM.

the problem is one-dimensional. They are exactly zero for the choice $\lambda_{\max}$ as it exactly preserves this property of the solution. This also explains why displacements have no effect on the error with $\lambda_{\max}$. Errors are greater as $\lambda$ takes smaller values because it increases the proportion of the cell faces allocated to non-existing interactions between the two materials.

### 3.4.3 Sand and shale

Finally, the more sophisticated sand and shale problem [27] is considered. The domain $[0,1]\times[0,0.5]$ is filled with a high conductivity $\kappa_1=1$ medium (the sand) and small squares of a insulating $\kappa_2=0$ material (the shale). The squares are of dimension $0.05\times0.05$ and are randomly generated throughout the domain as in Fig. 9. Temperature is equal to $T=4$ at the bottom and $T=0$ at the top. Fluxes are set to zero along the left and right borders.

With a sufficiently fine mesh, this test case locally resembles the sandwich problem. The qualitative results are expected to be similar, preserving the previously exposed hierarchy of the different methods. Such a fine mesh can however be out of reach if the structures of interest are especially small. Looking at the results for coarser meshes is then required. Here a $80\times40$ mesh (i.e. 4 cells along each square side) is used and the results are compared with a reference solution computed on a $1000\times500$ mesh. Once again, the number of cells is chosen so as to ensure that the unperturbed meshes consist only of pure cells. The final time is $t=1$ with a time step of $\Delta t=0.1$.

Results are given in Fig. 10 for horizontal, vertical and diagonal displacement of the mesh. Once again, homogenized method does not fare well, regardless of the chosen mean and the DEM performs better. Linear reconstruction slightly reduces the error most of the time but the more significant parameter seems to be the choice of $\lambda$. The choice $\lambda_{\min}$ is by far the worst of the three. The choices $\lambda_0$ and $\lambda_{\max}$ yield comparable results, $\lambda_0$ being more robust to horizontal displacements and $\lambda_{\max}$ to vertical ones. Strikingly, with vertical and diagonal displacements, both give a lower error than for the pure cell case

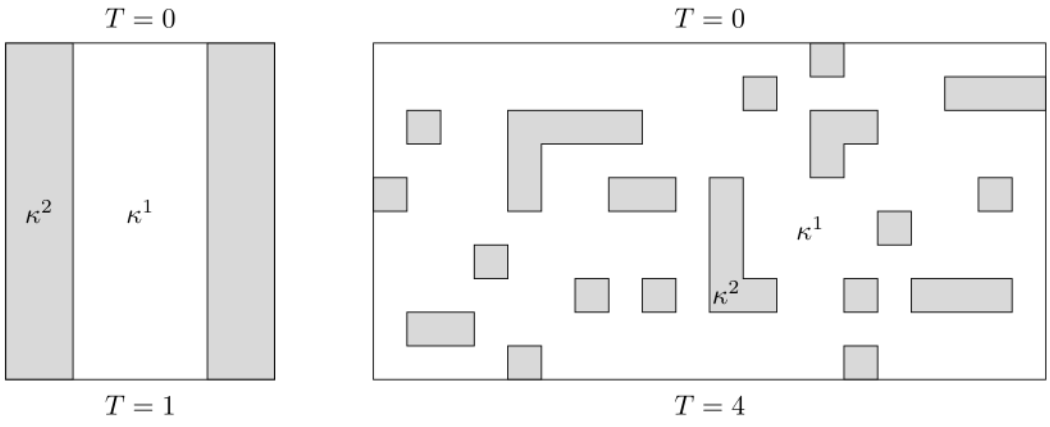


Figure 9: Sandwich (left) and sand and shale (right) configurations.

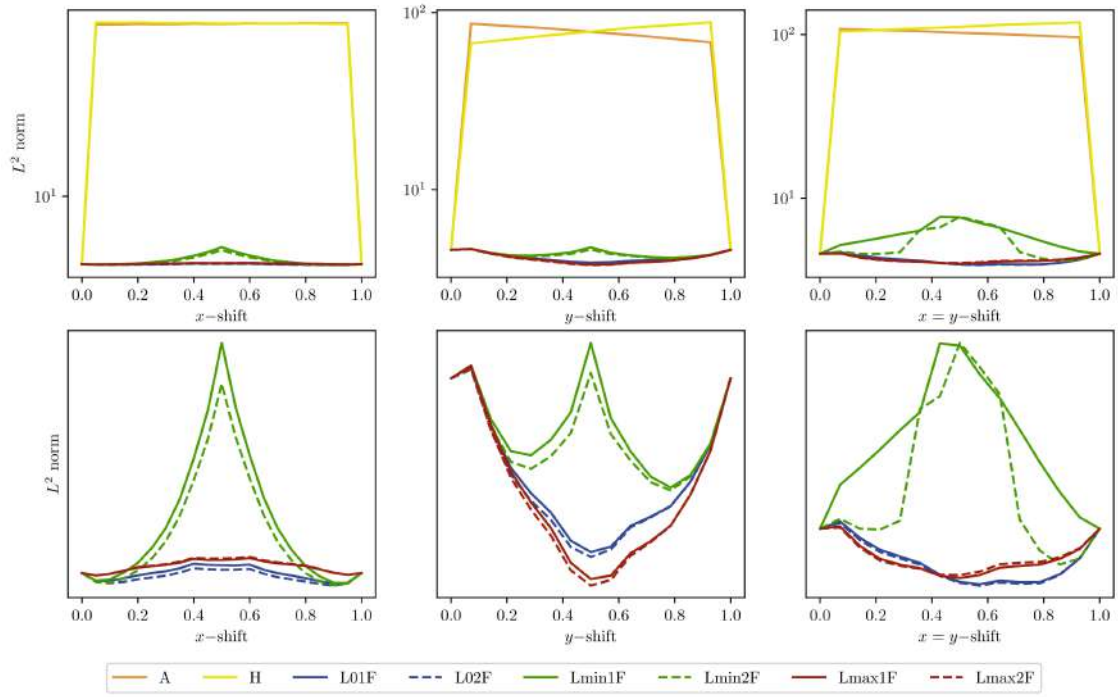


Figure 10: $L^2$ error for the sand and shale problem as a function of the horizontal (left), vertical (middle) or diagonal (right) displacement of the mesh. Top: for all methods. Bottom: only for the DEM.

(i.e. for a relative displacement of 0 or 1) which means that the presence of mixed cell does actually improve the results.

### 3.5 Intermediate conclusion

The three previous test cases illustrate the proficiency of the DEM. It fares significantly better than the homogeneous methods. Concerning the different options and parameters, several comments can be made.

- Out of the three values of $\lambda, \lambda_{\min}$ gives the worst results while $\lambda_0$ and $\lambda_{\max}$ are mostly equivalent on the sand and shale test case.
- The internal flux may improve the results on coarse meshes (although not automatically) but its effect eventually disappears on finer ones. It is then arguably reasonable to neglect it all together and to gloss over the difficulties related to its expression.
- Finally, linear reconstruction of volume fractions improve results most of the time compared to a constant reconstruction. However, the effect seems to be mostly negligible on sophisticated test cases.

As such, the choice of $\lambda_0$ with constant reconstruction of volume fraction and no internal flux (L01F) is overall a sensible choice. It is the simplest one, gives better results than $\lambda_{\min}$, avoid the singularities of $\lambda_{\max}$ or high order reconstructions (as explained in Section 3.2.3), and its formulation easily extends to an arbitrary number of materials. This choice will be retained for the test cases of the following section.

# 4 A cell-centered Lagrangian scheme for three-temperature multi-material hydrodynamics

A new scheme is now presented for the three-temperature multi-material equations (2.8). One of the main building block of this strategy is the approximation of the radiation diffusion with the method developed in the previous section.

## 4.1 Space discretization

### 4.1.1 Hydrodynamics

The hydrodynamics part of the scheme consists in a multi-material extension of the GLACE/EUCCLHYD schemes [5, 31]. Global quantities (i.e. total Lagrangian volume, momentum and total energy of the system) are solved with the single-material scheme. The scheme is here written in internal energy as opposed to the usually preferred total energy. The internal energy formulation lays the necessary foundations for a thermodynamically consistent space discretization of the material quantities

$$m_c^k \frac{\mathrm{d}}{\mathrm{d}t}\left(\frac{1}{(\alpha\rho)_c^k}\right) = \sum_{p\in\mathcal{P}(c)} l_{pc}\mathbf{n}_{pc}\cdot\mathbf{u}_p, \tag{4.1a}$$

$$m_c \frac{\mathrm{d}}{\mathrm{d}t}\mathbf{u}_c = \sum_{p\in\mathcal{P}(c)} \mathbf{M}_{pc}\left(\mathbf{u}_p - \mathbf{u}_c\right), \tag{4.1b}$$

$$\sum_k m_c^k \frac{\mathrm{d}}{\mathrm{d}t} e_c^k = -p_c \sum_{p\in\mathcal{P}(c)} l_{pc}\mathbf{n}_{pc}\cdot\mathbf{u}_p + Q_c, \tag{4.1c}$$

$$e_c^k = e_{i,c}^k + e_{e,c}^k + \frac{e_{r,c}^k}{\rho_c^k}, \tag{4.1d}$$

$$Q_c = \sum_{p\in\mathcal{P}(c)} (\mathbf{u}_p - \mathbf{u}_c)\cdot\mathbf{M}_{pc}(\mathbf{u}_p - \mathbf{u}_c), \tag{4.1e}$$

$$\mathbf{u}_p = \mathrm{M}_p^{-1} \sum_{c\in\mathcal{C}(p)} (\mathbf{M}_{pc}\mathbf{u}_p + p_c l_{pc}\mathbf{n}_{pc}). \tag{4.1f}$$

Eq. (4.1a) governs the evolution of the total Lagrangian volume. It is often referred to as the geometric conservation law [40]. Eq. (4.1b) is the conservation of momentum while (4.1c) is the total internal energy equation. $Q_c$ corresponds to the total irreversible heat

deposit of the scheme; the matrices $\mathbf{M}_{pc}$ are symmetric positive, thus ensuring $Q_c \geq 0$ and preventing destruction of entropy. The expressions (4.1e) and (4.1f) also enforce both consistency of the scheme and conservation of total energy. Details may be found in [15, 32]. The extension to a multi-material setting focuses on the discretization of individual densities, internal energies and entropies. For the sake of thermodynamical consistency, they are related to each other through Gibbs identity

$$\frac{\mathrm{d}}{\mathrm{d}t}e_{i,c}^k = -p_{i,c}^k \frac{\mathrm{d}}{\mathrm{d}t}\left(\frac{1}{\rho_c^k}\right) + T_{i,c}^k \frac{\mathrm{d}}{\mathrm{d}t}s_{i,c}^k, \tag{4.2a}$$

$$\frac{\mathrm{d}}{\mathrm{d}t}e_{e,c}^k = -p_{e,c}^k \frac{\mathrm{d}}{\mathrm{d}t}\left(\frac{1}{\rho_c^k}\right) + T_{e,c}^k \frac{\mathrm{d}}{\mathrm{d}t}s_{e,c}^k, \tag{4.2b}$$

$$\frac{\mathrm{d}}{\mathrm{d}t}\left(\frac{e_{r,c}^k}{\rho_c^k}\right) = -p_{r,c}^k \frac{\mathrm{d}}{\mathrm{d}t}\left(\frac{1}{\rho_c^k}\right) + T_{r,c}^k \frac{\mathrm{d}}{\mathrm{d}t}s_{r,c}^k \tag{4.2c}$$

in such a way that is compatible with (4.1c). Densities evolve according to the equal-strain assumption (2.10)

$$m_c^k \frac{\mathrm{d}}{\mathrm{d}t}\left(\frac{1}{\rho_c^k}\right) = \alpha_c^k \sum_{p\in\mathcal{P}(c)} l_{pc}\mathbf{n}_{pc}\cdot\mathbf{u}_p. \tag{4.3}$$

It is also equivalent to $\mathrm{d}\alpha_c^k/\mathrm{d}t = 0$. As for the entropy, the global heat deposit $Q$ can be shared arbitrarily between materials and their temperatures with respect to coefficients $\lambda_\theta^k$, $\theta \in \{i,e,r\}$

$$m_c^k T_c^k \frac{\mathrm{d}}{\mathrm{d}t}s_{\theta,c}^k = \lambda_{\theta,c}^k Q_c, \tag{4.4a}$$

$$\sum_k \sum_{\theta\in\{e,i,r\}} \lambda_{\theta,c}^k = 1. \tag{4.4b}$$

Changing the coefficients $\lambda_\theta^k$ changes the numerical approximation of shocks, even at convergence [1, 29]. Their expression must then be motivated by physics and cannot be reasonably specified by numerical considerations alone. The coefficients $\lambda^k = \lambda_i^k + \lambda_e^k + \lambda_r^k$ depend on the mixture (separated, dispersed …) and all the underlying small-scale phenomena (viscosity, surface tension, heat exchange …). Once the $\lambda^k$ are known, they should be divided into $\lambda_\theta^k$. Strictly speaking, the $\lambda_\theta^k$ can be arbitrary (as long as they sum up to $\lambda^k$) but they are here defined proportionally to the mass of the different species as prescribed in [43]

$$\lambda_\theta^k = \frac{m_\theta^k}{m^k}\lambda^k. \tag{4.5}$$

Then the ions bear almost all of the dissipation and the photons none.

### 4.1.2 Radiation transport and source terms

Local relaxation terms are approximated with a simple quadrature rule

$$\int_{\omega_c} \alpha^k c\kappa^k \left(T_e^k - T_i^k\right) \simeq c V_c^k \kappa_c^k \left(T_{e,c}^k - T_{i,c}^k\right), \tag{4.6a}$$

$$\int_{\omega_c} \alpha^k c\sigma_P^k \left(a\left(T_r^k\right)^4 - a\left(T_e^k\right)^4\right) \simeq c V_c^k \sigma_{P,c}^k \left(a\left(T_{r,c}^k\right)^4 - a\left(T_{e,c}^k\right)^4\right). \tag{4.6b}$$

Each relaxation term appears twice with opposite sign and the discretization of the opposite is the opposite of the discretization. This is both natural and necessary for energy conservation. Radiation transport is discretized with one of the strategies presented in Section 3. The previous thermal conductivities $\kappa$ are replaced with local approximations of opacities

$$\left[\frac{c}{3\sigma_R^k}\right]_c = \frac{c}{3\sigma_{R,c}^k}. \tag{4.7}$$

In the following, the discrete diffusion operator for material $k$ will be written in the generic form

$$\sum_{d,l} A_{cd}^{kl} \left(e_{r,c}^k - e_{r,d}^l\right) \tag{4.8}$$

with $A_{cd}^{kl} \geq 0$ depending on the chosen strategy and the geometry of the mesh. Eventually, the semi-discrete internal energy equations read

$$m_c^k \frac{\mathrm{d}}{\mathrm{d}t} e_{i,c}^k = H_{i,c}^k + c V_c^k \kappa_c^k \left(T_{e,c}^k - T_{i,c}^k\right), \tag{4.9a}$$

$$m_c^k \frac{\mathrm{d}}{\mathrm{d}t} e_{e,c}^k = H_{e,c}^k + c V_c^k \kappa_c^k \left(T_{i,c}^k - T_{e,c}^k\right) + c V_c^k \sigma_{P,c}^k \left(a\left(T_{r,c}^k\right)^4 - a\left(T_{e,c}^k\right)^4\right), \tag{4.9b}$$

$$m_c^k \frac{\mathrm{d}}{\mathrm{d}t} \frac{e_{r,c}^k}{\rho_c^k} = H_{r,c}^k + \sum_{d,l} A_{cd}^{kl} \left(e_{r,d}^l - e_{r,c}^k\right) + c V_c^k \sigma_{P,c}^k \left(a\left(T_{e,c}^k\right)^4 - a\left(T_{r,c}^k\right)^4\right) \tag{4.9c}$$

with $H_{i,c}^k$, $H_{e,c}^k$ and $H_{r,c}^k$ the previously detailed, discretization of the hydrodynamic part

$$H_{\theta,c}^k = -\alpha_c^k p_{\theta,c}^k \sum_{p \in \mathcal{P}(c)} l_{pc} \mathbf{n}_{pc} \cdot \mathbf{u}_{pc} + \lambda_{\theta,c}^k Q_c. \tag{4.10}$$

**Remark 4.1.** In the present document, diffusion is only considered for radiation temperature. However, diffusion could also be added on the ionic and electronic temperatures. In this case, the DEM derived in the previous section can be applied on each diffusion operator. The time implicit integration detailed in the following only deals with radiation diffusion but a splitting can still be used for the ionic and electronic ones.

### 4.2 Implicit time integration: An iterative method based on convex combinations

Temperature relaxation processes and radiation transport are usually stiff phenomena. Explicit time integration of these terms is possible but would require unreasonably small time steps. An implicit integration is then preferred so that only the hydrodynamics part of the scheme constrains the time steps

$$\frac{m_c^k}{\Delta t}\left(e_{i,c}^{k,n+1}-e_{i,c}^{k,n}\right)=H_{i,c}^{k,n}+c(V\kappa)_c^{k,n+1}\left(T_{e,c}^{k,n+1}-T_{i,c}^{k,n+1}\right), \tag{4.11a}$$

$$\begin{aligned}\frac{m_c^k}{\Delta t}\left(e_{e,c}^{k,n+1}-e_{e,c}^{k,n}\right)&=H_{e,c}^{k,n}+c(V\kappa)_c^{k,n+1}\left(T_{i,c}^{k,n+1}-T_{e,c}^{k,n+1}\right)\\&\quad+c(V\sigma_P)_c^{k,n+1}\left(a\left(T_{r,c}^{k,n+1}\right)^4-a\left(T_{e,c}^{k,n+1}\right)^4\right),\end{aligned} \tag{4.11b}$$

$$\begin{aligned}\frac{m_c^k}{\Delta t}\left(\frac{e_{r,c}^{k,n+1}}{\rho_c^{k,n+1}}-\frac{e_{r,c}^{k,n}}{\rho_c^{k,n}}\right)&=H_{r,c}^{k,n}+\sum_{d,l}A_{cd}^{kl,n+1}\left(e_{r,d}^{l,n+1}-e_{r,c}^{k,n+1}\right)\\&\quad+c(V\sigma_P)_c^{k,n+1}\left(a\left(T_{e,c}^{k,n+1}\right)^4-a\left(T_{r,c}^{k,n+1}\right)^4\right)\end{aligned} \tag{4.11c}$$

with the hydrodynamics part

$$\begin{aligned}H_{\theta,c}^{k,n}&=-\alpha_c^{k,n}p_{\theta,c}^{k,n}\sum_{p\in\mathcal{P}(c)}l_{pc}^n\mathbf{n}_{pc}^n\cdot\mathbf{u}_{pc}^n\\&\quad+\lambda_{\theta,c}^{k,n}\sum_{p\in\mathcal{P}(c)}\left(\mathbf{u}_c^n-\mathbf{u}_p^n\right)\cdot\mathbf{M}_{pc}^n\left(\frac{1}{2}\left(\mathbf{u}_c^{n+1}+\mathbf{u}_c^n\right)-\mathbf{u}_p^n\right).\end{aligned} \tag{4.12}$$

**Remark 4.2.** In (4.12), it is necessary to take the half-sum $(\mathbf{u}^{n+1}+\mathbf{u}^n)/2$ for total energy conservation as explained in [11]. This is not an implicitation *per se* as momentum equations are solved before energy equations.

System (4.11) is non-linear as energies $e_i^k,e_e^k,e_r^k$ and coefficients $\kappa,\sigma_P,\sigma_R$ are possibly non-linear functions of temperatures. Following [10], it is then solved by an iterative strategy with which positivity of temperatures is ensured at each step (under some conditions detailed in Proposition 4.3). The number of the sub-iteration is indicated by the letter $m$. First, defining the new variables

$$\phi_\theta^k=aT_\theta^k, \qquad \forall\theta\in\{i,e,r\}, \tag{4.13a}$$

$$\beta_{\theta,c}^{k,n+1,m}=\frac{\phi_{\theta,c}^{k,n+1,m}-\phi_{\theta,c}^{k,n}}{e_{\theta,c}^{k,n+1,m}-e_{\theta,c}^{k,n}}, \quad \forall\theta\in\{i,e\}, \tag{4.13b}$$

$$\delta_{ie,c}^{k,n+1,m}=\frac{T_{i,c}^{k,n+1,m}-T_{e,c}^{k,n}}{\phi_{i,c}^{k,n+1,m}-\phi_{e,c}^{k,n+1,m}}, \tag{4.13c}$$

the linearized equations for the $m$-th iteration are

$$\begin{aligned}
&\frac{m_c^k}{\beta_{i,c}^{k,n+1,m}\Delta t}\left(\phi_{i,c}^{k,n+1,m+1}-\phi_{i,c}^{k,n}\right)\\
&=H_{i,c}^{k,n}+c(V\kappa\delta_{ie})_c^{k,n+1,m}\left(\phi_{e,c}^{k,n+1,m+1}-\phi_{i,c}^{k,n+1,m+1}\right), \qquad (4.14a)\\
&\frac{m_c^k}{\beta_{e,c}^{k,n+1,m}\Delta t}\left(\phi_{e,c}^{k,n+1,m+1}-\phi_{e,c}^{k,n}\right)\\
&=H_{e,c}^{k,n}+c(V\kappa\delta_{ie})_c^{k,n+1,m}\left(\phi_{i,c}^{k,n+1,m+1}-\phi_{e,c}^{k,n+1,m+1}\right)\\
&\quad+c(V\sigma_P)_c^{k,n+1,m}\left(\phi_{r,c}^{k,n+1,m+1}-\phi_{e,c}^{k,n+1,m+1}\right), \qquad (4.14b)\\
&\frac{m_c^k}{\Delta t}\left(\frac{\phi_{r,c}^{k,n+1,m+1}}{\rho_c^{k,n+1}}-\frac{\phi_{r,c}^{k,n}}{\rho_c^{k,n}}\right)\\
&=H_{r,c}^{k,n}+\sum_{d,l}A_{cd}^{kl,n+1,m}\left(\phi_{r,d}^{l,n+1,m+1}-\phi_{r,c}^{k,n+1,m+1}\right)\\
&\quad+c(V\sigma_P)_c^{k,n+1,m}\left(\phi_{e,c}^{k,n+1,m+1}-\phi_{r,c}^{k,n+1,m+1}\right). \qquad (4.14c)
\end{aligned}$$

Without the diffusion, system (4.14) would only be a concatenation of $3\times3$ linear systems for each cell and each material. Diffusion couples all these systems both spatially and in between materials so that a global matrix inversion cannot be avoided. Instead of directly solving (4.14), the local $3\times3$ systems are first analytically triangularized so that the global system now only concerns the radiation temperatures. This effectively divides by 3 the size of the linear system to be inverted. The triangularization reveals the following convex combinations:

$$\begin{aligned}
&\phi_{i,c}^{k,n+1,m+1}=h_c^{k,n+1,m}\psi_{i,c}^{k,n+1,m}+\left(1-h_c^{k,n+1,m}\right)\phi_c^{k,n+1,m}, \qquad (4.15a)\\
&\phi_{e,c}^{k,n+1,m+1}=f_c^{k,n+1,m}\left(\psi_{e,c}^{k,n+1,m}+\left(1-g_c^{k,n+1,m}\right)\psi_{i,c}^{k,n+1,m}\right)\\
&\qquad+\left(1-f_c^{k,n+1,m}\right)\phi_{r,c}^{k,n+1,m+1}, \qquad (4.15b)\\
&\phi_{r,c}^{k,n+1,m+1}\left(\frac{m_c^k}{\rho_c^{k,n}}+\Delta tc(V\sigma_P f)_c^{k,n+1,m}+\sum_{d,l}A_{cd}^{kl,n+1,m}\right)-\sum_{d,l}A_{cd}^{kl,n+1,m}\phi_{r,d}^{l,n+1,m+1}\\
&=m_c^k\psi_{r,c}^{k,n+1,m}+\Delta tc(V\sigma_P f)^{k,n+1,m}\left(\psi_{e,c}^{k,n+1,m}+\left(1-g_c^{k,n+1,m}\right)\psi_{i,c}^{k,n+1,m}\right), \qquad (4.15c)
\end{aligned}$$

where

$$\begin{aligned}
h_c^{k,n+1,m}&=\frac{1}{1+c(V\kappa\delta_{ie}\beta_i)_c^{k,n+1,m}\Delta t/m_c^k}, \qquad (4.16a)\\
g_c^{k,n+1,m}&=\frac{1}{1+c(V\kappa\delta_{ie}\beta_e h)_c^{k,n+1,m}\Delta t/m_c^k}, \qquad (4.16b)\\
f_c^{k,n+1,m}&=\frac{1}{1+c(V\sigma_P\beta_e g)\Delta t/m_c^k}, \qquad (4.16c)
\end{aligned}$$

and

$$\psi_{i,c}^{k,n+1,m} = \phi_{i,c}^{k,n} + \frac{\Delta t \beta_{i,c}^{k,n+1,m}}{m_c^k} H_{i,c}^{k,n}, \tag{4.17a}$$

$$\psi_{e,c}^{k,n+1,m} = \phi_{e,c}^{k,n} + \frac{\Delta t \beta_{e,c}^{k,n+1,m}}{m_c^k} H_{e,c}^{k,n}, \tag{4.17b}$$

$$\psi_{r,c}^{k,n+1,m} = \frac{\phi^{k,n}}{\rho^{k,n}} + \frac{\Delta t}{m_c^k} H_{r,c}^{k,n}. \tag{4.17c}$$

The numerical time step $\Delta t$ is not restricted by the radiation transport or the source terms. It is only driven by the hydrodynamic part of the equations and its resulting CLF-like condition

$$\frac{\Delta t c_c}{V_c} P_c \leq \frac{1}{2}, \tag{4.18}$$

where $V_c$ is the volume of the cell, $P_c$ its perimeter and $c_c$ the mixture speed of sound (2.12). This restriction is supplemented with a second restriction preventing cell inversion and thus ensuring positivity of the density.

**Remark 4.3.** Strictly speaking, system (4.15) consists in convex combinations if and only if coefficients $\beta_{i,c}^{k,n+1,m}$ and $\beta_{e,c}^{k,n+1,m}$ are non-negative. For a given equation of state, the heat capacity $c_v$ and the Grüneisen coefficient $\Gamma$ are defined as

$$c_v = \left.\frac{\partial e}{\partial T}\right|_\rho, \tag{4.19a}$$

$$\Gamma = \left.\frac{\rho}{T}\frac{\partial T}{\partial \rho}\right|_s. \tag{4.19b}$$

The following thermodynamic relation then stands:

$$\mathrm{d}T = \frac{1}{c_v}\mathrm{d}e + \left(\frac{p}{c_v} - \rho\Gamma T\right)\mathrm{d}\left(\frac{1}{\rho}\right). \tag{4.20}$$

Eq. (4.20) is in particular valid for the equation of state of ions and electrons of material $k$. Because $c_{v,i}^k > 0$ and $c_{v,e}^k > 0$, coefficients $\beta_{i,c}^{k,n+1,m}$ and $\beta_{e,c}^{k,n+1,m}$ are always positive as long as the variation of volume is neglected. If not, these coefficients may become negative and convex combinations are lost. Radiation phenomena usually occurs on time scales shorter than those of hydrodynamics so that variations of volume can be reasonably neglected.

**Remark 4.4.** The convergence rate of the present method is slower than a regular Newton's method. Although Newton's method may fail to ensure positivity of temperatures and may thus crash the simulation in demanding test cases [10], it usually behaves well. The present method should not be seen as the main procedure but rather as a backup to another faster-converging method.

### 4.2.1 Properties

**Proposition 4.1** (Discrete Energy Conservation)**.** The discrete total energy

$$\sum_c \left[ m_c \frac{\|\mathbf{u}_c\|^2}{2} + \sum_k m_c^k \left( e_{i,c}^{k,n} + e_{e,c}^{k,n} + \frac{e_{r,c}^{k,n}}{\rho_c^{k,n}} \right) \right] \tag{4.21}$$

is conserved.

*Proof.* When summing ionic, electronic and radiation energy, the contribution of relaxation terms disappears. Radiation transport is written in terms of fluxes which cancel when summed over all cells and all materials as explained in Section 3.3. Only remains the hydrodynamics part. Conservation is not obvious in (4.1) where the internal energy formulation was favored. Proof of the conservation of total energy (as well as momentum) for the GLACE/EUCCLHYD scheme can be found in [5, 16, 31, 32]. □

**Proposition 4.2** (Semi-Discrete Entropy Production)**.** The following semi-discrete inequality on total entropy stands:

$$\sum_{c,k} m_c^k \frac{\mathrm{d}}{\mathrm{d}t} \left( s_{i,c}^k + s_{e,c}^k + s_{r,c}^k \right) \geq 0. \tag{4.22}$$

*Proof.* The semi-discrete entropy equations read

$$m_c^k T_{i,c}^k \frac{\mathrm{d}}{\mathrm{d}t} s_{i,c}^k = \lambda_{i,c}^k Q_c + c(V\kappa)_c^k \left( T_{e,c}^k - T_{i,c}^k \right), \tag{4.23a}$$

$$m_c^k T_{e,c}^k \frac{\mathrm{d}}{\mathrm{d}t} s_{e,c}^k = \lambda_{e,c}^k Q_c + c(V\kappa)_c^k \left( T_{i,c}^k - T_{e,c}^k \right) + c(V\sigma_P)_c^k \left( a\left(T_{e,c}^k\right)^4 - a\left(T_{r,c}^k\right)^4 \right), \tag{4.23b}$$

$$m_c^k T_{r,c}^k \frac{\mathrm{d}}{\mathrm{d}t} s_{r,c}^k = \lambda_{r,c}^k Q_c + \sum_{d,l} A_{cd}^{kl} \left( e_{r,d}^l - e_{r,c}^k \right) + c(V\sigma_P)_c^k \left( a\left(T_{e,c}^k\right)^4 - a\left(T_{r,c}^k\right)^4 \right). \tag{4.23c}$$

The relaxation terms provide a local and individual (i.e. for a given cell and a given material) entropy production as it can be seen by summing all equations of (4.23). Radiation transport, however, consists in a heat exchange between cells and materials so that the associated entropy production can only be recovered by summing equations (4.23c) over all cells and all materials. Eventually

$$\begin{aligned}
&\sum_{c,k} m_c^k \frac{\mathrm{d}}{\mathrm{d}t} \left( s_{i,c}^k + s_{e,c}^k + s_{r,c}^k \right) \\
&= \left( \sum_k \sum_{\theta \in \{i,e,r\}} \frac{\lambda_{\theta,c}^k}{T_{\theta,c}^k} \right) Q_c + \sum_{\{c,d\},\{k,l\}} A_{cd}^{kl} \frac{\left(T_{r,c}^k - T_{r,d}^l\right)\left(\left(T_{r,c}^k\right)^4 - \left(T_{r,d}^l\right)^4\right)}{T_{r,c}^k T_{r,d}^l} \\
&\quad + \sum_{c,k} c(V\kappa)_c^k \frac{\left(T_{i,c}^k - T_{e,c}^k\right)^2}{T_{i,c}^k T_{e,c}^k} + \sum_{c,k} ca(V\sigma_P)_c^k \frac{\left(T_{e,c}^k - T_{r,c}^k\right)\left(\left(T_{e,c}^k\right)^4 - \left(T_{r,c}^k\right)^4\right)}{T_{e,c}^k T_{r,c}^k},
\end{aligned} \tag{4.24}$$

which is, as announced, non-negative. □

**Proposition 4.3** (Positivity of Temperatures)**.** Under a hydrodynamics-driven CFL condition and the positivity of coefficients $\beta_{i,c}^{k,n+1,m}$ and $\beta_{e,c}^{k,n+1,m}$, temperatures stay positive at each step of the iterative procedure.

*Proof.* If coefficients $\beta_{i,c}^{k,n+1,m}$ and $\beta_{e,c}^{k,n+1,m}$ are positive, coefficients $h$,$g$ and $f$ (4.16) belong to $[0,1]$. On the other hand, all $\psi$ (4.17) variables are positive under a CFL-like condition which only depends on the hydrodynamics. Then, the right-hand side of Eq. (4.15c) is positive. The global matrix associated to the left-hand side of system (4.15c) is a $M-$matrix. Consequently, positivity of radiation temperatures is ensured. Finally, positivity of electronic and ionic temperatures follows from the convex combinations (4.15b) and (4.15a). □

## 4.3 Numerical results

Two test cases are presented in this section. No analytical solution can be given considering the complexity of the equations, the non-linearity of coefficients and the non-uniqueness of shocks. Numerical results can still be qualitatively compared with the ones presented in [9, 17, 39].

## 4.4 Ablation wall problem

For this one-dimensional test case [39], a hot gas (xenon) interacts with a denser cold wall (beryllium). The radiation transport at the interface heats the beryllium and triggers an expansion wave pushing the interface towards the hot gas. Additionally, the initial pressure discontinuity generates a shock wave through the gas while the pressure difference induced by the heating of the wall causes a second shock wave to propagate inside it. The resulting physical setting is extremely stiff because of the high contrast in densities, pressures, temperatures and opacities. In particular, opacity experiences a sharp change at the interface ($\sigma_R/\sigma_L \approx 10^{12}$). The domain measures 0.16 cm and is initially divided at $x = 0.10$ cm with the wall on the right. Initial quantities are summarized in Table 1 along with the values of the physical constants. In practice, the present three-temperature code is reduced to a two-temperature one by using infinite $\kappa$ ($10^{30}$ for both materials in our test) and taking $(c_v)_i = (c_v)_e = c_v/2$.

The numerical results are displayed in Fig. 11 for the Lagrangian simulations and in Fig. 12 for the Lagrange+Remap (indirect Eulerian) formalism. It is observed that both converge toward the same solution. However, when comparing these results with the aforementioned references, large differences in the numerical profiles are observed; here, the diffusion seems frozen. This explains why the temperature is lower on the right side of the wall; the beryllium experiences an expansion whose resulting temperature decrease is not compensated by the heat flux from the xenon. Radiation still has an effect on the left part of the solution where the opacity is quite low; the equilibration of material and radiation temperatures lags. As stated earlier, opacities $\sigma_R$ and $\sigma_L$ are extremely different so taking the harmonic mean in (3.15c) essentially gives the smaller conductivity

Table 1: Initial conditions of the ablation wall problem.

| | Unit | Xenon | Beryllium |
|---|---|---|---|
| $\rho$ | $\mathrm{g.cm^{-3}}$ | 0.006 | 1.85 |
| $u$ | $\mathrm{cm.s^{-1}}$ | 0 | 0 |
| $k_BT = k_BT_r$ | eV | 100 | 1 |
| $p$ | $\mathrm{g.cm^{-1}.s^{-2}}$ | $(\gamma-1)\rho e$ | |
| $e$ | $\mathrm{erg.g^{-1}}$ | $c_v(k_BT)$ | |
| $e_r$ | $\mathrm{erg.cm^{-3}}$ | $a(k_BT_r)^4$ | |
| $\sigma_P = \sigma_R$ | $\mathrm{cm^{-1}}$ | $\sigma_0\rho^2(k_BT)^{-7/2}$ | |
| $c_v$ | $\mathrm{cm^2.s^{-2}.eV^{-1}}$ | $3.22\cdot10^{11}$ | $7.98\cdot10^{11}$ |
| $\gamma$ | | 5/4 | 5/3 |
| $\sigma_0$ | $\mathrm{cm^{-1}}$ | $3.1\cdot10^{8}$ | $4.2\cdot10^{9}$ |
| $c$ | $\mathrm{cm.s^{-1}}$ | $3.00\cdot10^{10}$ | |
| $k_B$ | $\mathrm{eV.K^{-1}}$ | $8.61\cdot10^{-5}$ | |
| $a$ | $\mathrm{erg.cm^{-3}.eV^{-4}}$ | $1.37\cdot10^{2}$ | |

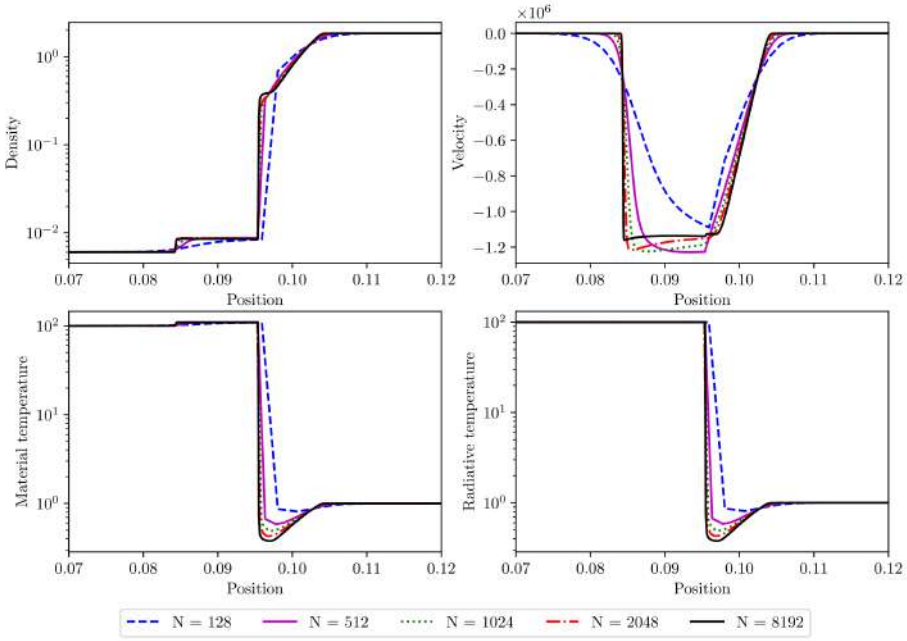


Figure 11: Results at 4ns of the ablation wall problem (see Table 1) for different meshes working in a Lagrangian formalism and the DEM presented in (3.15c).

of the two. Consequently, the observed convergence is only that of the pressure-based part of the equation and the diffusion part has not yet kicked in. Because the flux is proportional to $\kappa/\Delta x$, a small enough mesh spacing $\Delta x$ will eventually trigger diffusion.

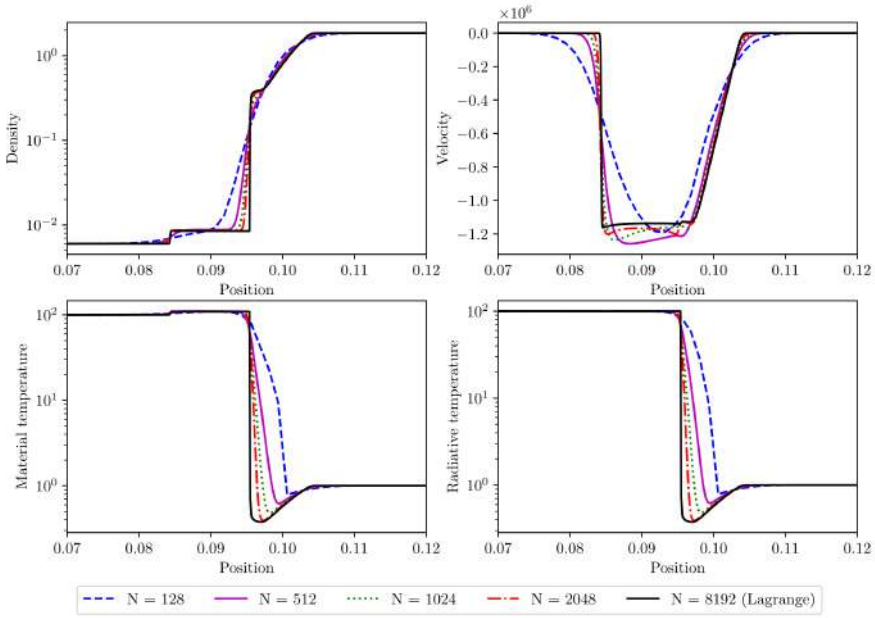


Figure 12: Results at 4ns of the ablation wall problem (see Table 1) for different meshes working in a Lagrange+Remap formalism and the DEM presented in (3.15c).

Such a fine mesh is however not accessible in practice and full convergence cannot be observed.

A more sensible approach would then be to define the interface opacity so that its effect on coarse meshes reproduces the small-scale behavior; note that this strategy is akin to the approximation of non-conservative products where the numerical diffusion is shaped to mimic small-scale dissipation processes. Alternatively to the harmonic averaging in (3.15c), arithmetic or geometric means can be used and the different results are compared in Fig. 13. All solutions, except for the harmonic mean, display a similar structure which is consistent with the semi-analytical solution given in [17] and the numerical results obtained in [9, 39]. However, the previously published results as well as the present ones all display different wave and interface positions between each other. This is expected as the intrinsic numerical diffusion of each scheme is different and affects the approximation of shocks as well as the balance between hydrodynamic and diffusion time scales. How to define the proper interface opacity is way beyond the aim of this article as it would require an ad hoc approach to carefully compare these time scales.

Finally, beyond the present numerical strategy, another issue concerns the relevance of the model itself. The diffusion approximation indeed only makes sense in the optically-thick limit; more sophisticated models (with a full radiation transfer description, encompassing all possible regimes including the optically-thin one) and related numerical methods (e.g. multi-scale approaches [30]) would be required for a more physically accurate description.

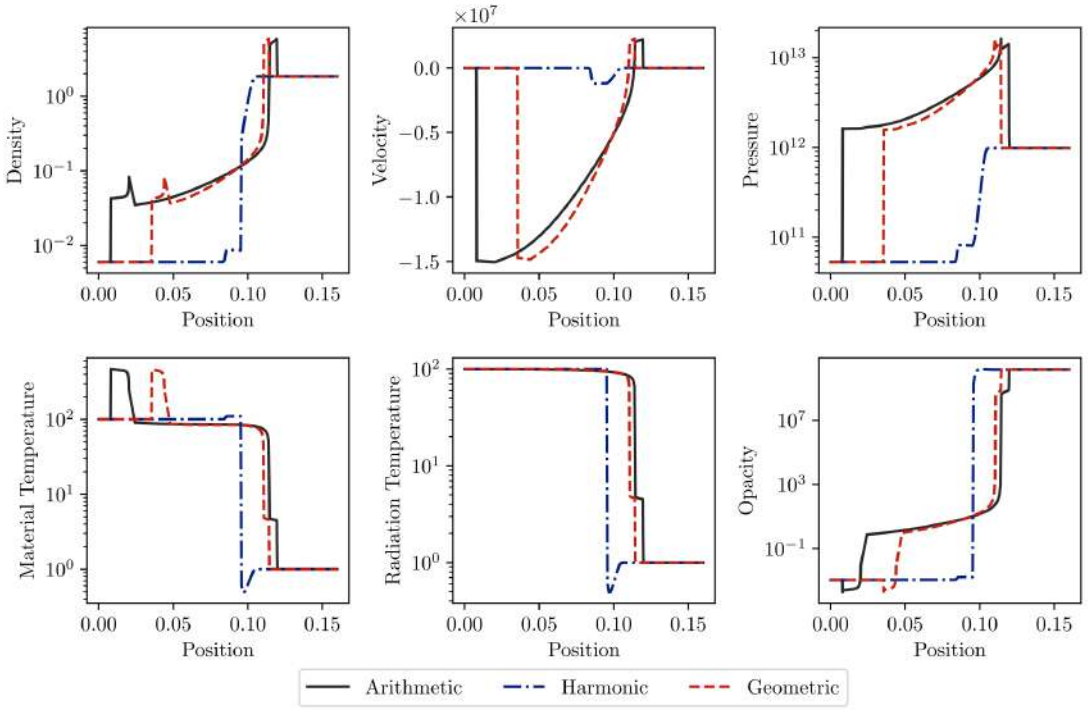


Figure 13: Results at 4ns of the ablation wall problem (see Table 1) for Lagrangian simulations with 1024 cells and different interface averages for the diffusion coefficient.

### 4.5 Two-dimensional test case

The last test case comes from [9] and is itself inspired from the one found in [36]. Results can not be compared directly to these references as the dimensions and equations of state are not specified in the former one while the latter one does not take into account hydrodynamics. In any case, this test case aims at demonstrating the proficiency of the present scheme in a two-dimensional setting. A more quantitative approach is out of the scope of this work. Here two configurations are studied. In the first one, the three-temperature model is reduced to a two-temperature one by using an infinite electron-ion relaxation parameter ($\kappa = 10^{30}$ in practice) for both materials. In the second one, a small electron-ion relaxation parameter $\kappa = 0.1$ is chosen. For both configurations heat capacities are set to $(c_v)_i = (c_v)_e = c_v/2$.

The two materials initially occupy the domain $[0,1]\times[0,1]$ as in Fig. 14 with a radial temperature distribution

$$T(x,y) = T_r(x,y) = \left(0.001 + 100\exp\left(-\frac{x^2+y^2}{0.01}\right)\right)^{\frac{1}{4}}, \tag{4.25}$$

a constant density $\rho = 1$ and a constant velocity $\mathbf{u} = \mathbf{0}$. Both the speed of light $c$ and the

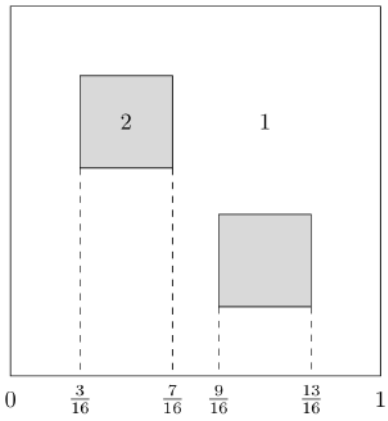


Figure 14: Configuration of the two-dimensional two-temperature two-material problem. The dimensions on the $y$-axis can be recovered from the symmetry with respect to the line $x=y$.

radiation constant $a$ are set to 1. The two materials are two identical perfect gases with $\Gamma^1=\Gamma^2=0.4$. Their opacity however differ from each other. They are expressed as

$$\sigma_R=\sigma_P=\frac{z}{T^3} \tag{4.26}$$

with $z=0.1$ for the first material and $z=1$ for the second. Symmetric boundary conditions are set to the left and bottom borders while zero Neumann conditions are set to the top and right borders. Results at $t=0.5$ for a $128\times128$ mesh are given in Fig. 15 for the first configuration (infinite electron-ion relaxation parameter) and in Fig. 16 for the second one ($\kappa=0.1$). The choice $\lambda_0$ with no internal flux and constant reconstruction of volume fraction is made for the radiation transport. The initial stiff temperature distribution evolves

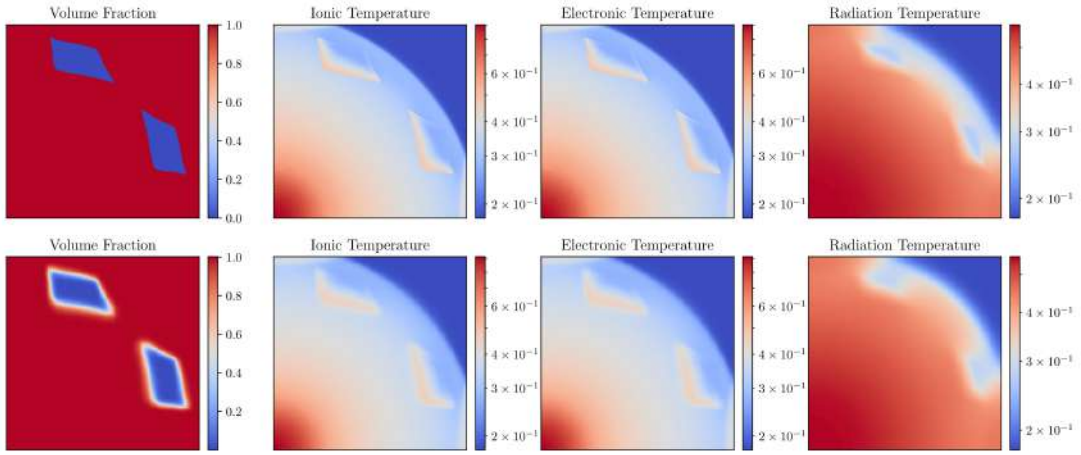


Figure 15: Results of the Mousseau-Knoll-Chauveheid test case at $t=1$ and for a $128\times128$ mesh with an infinite ion-electron relaxation parameter ($\kappa=10^{30}$). Top: without remapping. Bottom: with remapping.

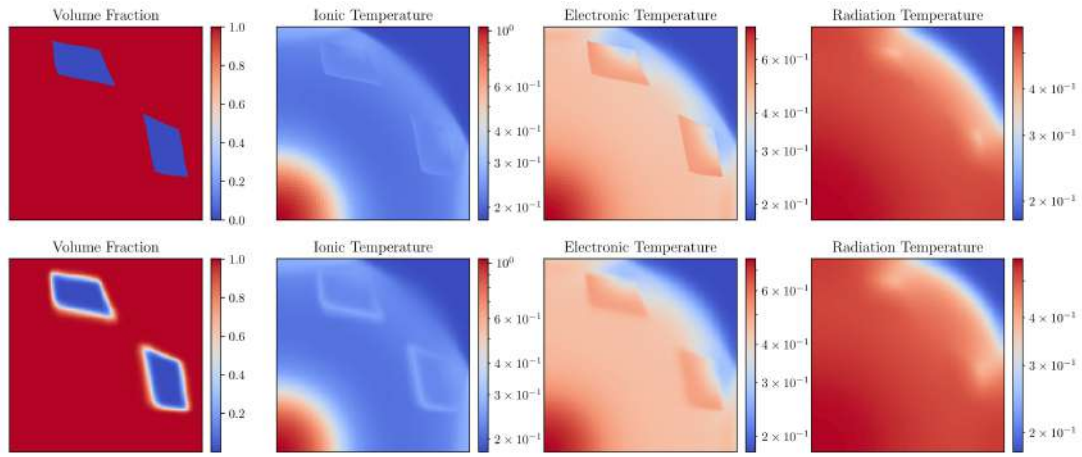


Figure 16: Results of the Mousseau-Knoll-Chauveheid test case at $t=1$ and for a $128\times128$ mesh with a small ion-electron relaxation parameter ($\kappa = 0.1$). Top: without remapping. Bottom: with remapping.

according to two phenomena. First, radiation transport propagates the centrally concentrated heat to the rest of the domain. Second, at constant density, temperature gradients induce pressure gradients which accelerate the system radially. The initial squares are eventually deformed by the acceleration. Neglecting the interaction of the heat front with the top and right borders, the solution would display a radial symmetry were it not for the difference in opacity. Indeed, the second material being more opaque, radiation does not propagate well inside. Its greater opacity also means that material and radiation temperatures are more coupled. As a result, material 2 radiation temperature is lower than its surroundings. Yet, its material temperature is actually greater than that of material 1 whose coupling between material and radiation temperature is weaker. Results with and without remapping share the same global behavior although the remapping obviously smears the solution at the interface between the two materials.

## 5 Conclusion

A method for to the discretization of three-temperature multi-material hydrodynamics was presented. A large focus is put on the multi-material radiation transport which is here dealt with the so-called discrete equation method. When compared with homogenization methods on perturbed meshes, the DEM shows significant improvement in accuracy while remaining both conceptually and computationally simple. The global numerical scheme conserves mass, momentum and total energy. Implicit time integration allows for stiff relaxation terms and radiation transport without unreasonably small time steps. The retained strategy also ensures that temperatures stay positive during the iterative time integration procedure.

Perspectives are numerous; three of them are here mentioned. First, extension to higher order is desirable for better accuracy as the present scheme is only at first order both in time and space. Anti-diffusive methods could be used to prevent over-smearing of the interface when the scheme is paired with a remapping procedure. Second, the methodology of comparison with perturbed meshes could be extended and bettered for more general meshes (with random displacements for instance). Finally, even though the scheme is written for an arbitrary number of materials, it remains to check its efficiency for more than two materials.

# Appendix A Interface area proportions: Extension to more than two materials

This section extends the analysis exposed in Section 3.2.2 for system (3.7) (rewritten below) when dealing with an arbitrary number $N$ of materials

$$\sum_l \delta_{cd}^{kl} = \delta_{cd}^k, \quad \forall k, \tag{A.1a}$$

$$\sum_k \delta_{cd}^{kl} = \delta_{dc}^l, \quad \forall l. \tag{A.1b}$$

The set of unknowns may be gathered on the $N \times N$ array where the $(k,l)$-th entry is $\delta_{cd}^{kl}$. Then, Eq. (A.1a) constrain the sum of rows and (A.1b) the sum of columns. In Fig. 17 is displayed the matrix for $N = 3$. The array form of the equations substantially eases the analysis. It may be seen that a necessary and sufficient condition for (A.1) to have a solution is

$$\sum_k \delta_{cd}^k = \sum_l \delta_{dc}^l, \tag{A.2}$$

which is trivially satisfied because both sides of the equation are equal to one. In terms of linear algebra, it means that the image of the linear mapping related to (A.1) is the

$$\begin{array}{|ccc|c} \delta_{cd}^{11} & \delta_{cd}^{12} & \delta_{cd}^{13} & \delta_{cd}^1 \\ \delta_{cd}^{21} & \delta_{cd}^{22} & \delta_{cd}^{23} & \delta_{cd}^2 \\ \delta_{cd}^{31} & \delta_{cd}^{32} & \delta_{cd}^{33} & \delta_{cd}^3 \\ \hline \multicolumn{3}{c}{\delta_{dc}^1 \quad \delta_{dc}^2 \quad \delta_{dc}^3} & \end{array}$$

Figure 17: Matrix of variables for $N = 3$.

hyperplane defined by (A.2). The rank (i.e. the dimension of the image) is then $2N-1$. By the rank-nullity theorem, the kernel is then of dimension $N^2-(2N-1)=(N-1)^2$ which corresponds to the number of degrees of freedom on the solution. It is not surprising as setting the value of a $(N-1)\times(N-1)$ sub-array of the variable array is enough to fill up the rest with the conditions on the sum of the lines and columns. In the case $N=2$, there is only $(N-1)^2=1$ degree of freedom which corresponds to $\lambda$ in (3.9). The three cases $\lambda_0$,$\lambda_{\max}$ and $\lambda_{\min}$ do not all extend well to an arbitrary number of materials:

- An natural equivalent of $\lambda_0$ is given by

$$\delta_{cd}^{kl}=\delta_{cd}^{k}\delta_{dc}^{l}. \tag{A.3}$$

- The case $\lambda_{\max}$ consists in maximizing diagonals element in the variable matrix. A possible extension is

$$\delta_{cd}^{kk}=\min\left(\delta_{cd}^{k},\delta_{dc}^{k}\right), \tag{A.4a}$$

$$\delta_{cd}^{kl}=\frac{\left(\delta_{cd}^{k}-\delta_{cd}^{kk}\right)\left(\delta_{dc}^{l}-\delta_{cd}^{ll}\right)}{\sum_{k}\left(\delta_{cd}^{k}-\delta_{cd}^{kk}\right)}, \tag{A.4b}$$

  where (A.4a) corresponds to the maximum value diagonal elements can take. The rest of surface proportions are arbitrarily given by (A.4b), although other choices are still possible because of the great number of degrees of freedom.

- The case $\lambda_{\min}$ has no natural extension. Applying $\lambda_{\min}$ to every couple of materials is possible but heavily depends on the order with which couples are taken.

## References


[1] R. Abgrall and S. Karni, A comment on the computation of non-conservative products, *J. Comput. Phys.*, 229(8):2759–2763, 2010.

[2] R. Abgrall and R. Saurel, Discrete equations for physical and numerical compressible multiphase mixtures, *J. Comput. Phys.*, 186(2):361–396, 2003.

[3] R. A. Berry, R. Saurel, and O. Le Metayer, The discrete equation method (DEM) for fully compressible, two-phase flows in ducts of spatially varying cross-section, *Nucl. Eng. Des.*, 240(11):3797–3818, 2010.

[4] J. Breil, Numerical methods for Lagrangian and arbitrary-Lagrangian-Eulerian hydrodynamic contribution to the simulation of high-energy-density-physics problems, *Numerical Analysis [math.NA]*, Univresité de Bordeaux, 2016.

[5] G. Carré, S. Del Pino, B. Després, and E. Labourasse, A cell-centered Lagrangian hydrodynamics scheme on general unstructured meshes in arbitrary dimension, *J. Comput. Phys.*, 228(14):5160–5183, 2009.

[6] CEA DAM, 2020. `http://www-lmj.cea.fr`

[7] C. Chaigneau, Rapport CEA.

[8] C.-H. Chang and M.-S. Liou, A new approach to the simulation of compressible multifluid flows with AUSM$^+$ scheme, in: *16th AIAA Computational Fluid Dynamics Conference*, 4107, 2003.

[9] D. Chauveheid, *Ecoulements Multi-Matériaux et Multi-Physiques: Solveur Volumes Finis Eulérien Co-localisé Avec Capture D'interfaces, Analyse et Simulations*, PhD Thesis, Mathématiques Cachan, École normale supérieure, 2012.
[10] R. Chauvin, S. Guisset, B. Manach-Pérennou, and L. Martaud, A colocalized scheme for three-temperature grey diffusion radiation hydrodynamics, *Commun. Comput. Phys.*, 31(1):293–330, 2022.
[11] J. Cheng, C.-W. Shu, and Q. Zeng, A conservative Lagrangian scheme for solving compressible fluid flows with multiple internal energy equations, *Commun. Comput. Phys.*, 12:1307–1328, 2012.
[12] G. Dal Maso, P. Le Floch, and F. Murat, Definition and weak stability of nonconservative products, *J. Math. Pures Appl.*, 74:483–548, 1995.
[13] A. S. Dawes, Solving the diffusion equation on a non-aligned mesh, *Comput. & Fluids*, 83:77–89, 2013.
[14] A. S. Dawes, Three-dimensional multi-material polyhedral method for diffusion, *Comput.* & Fluids, 156:485–495, 2017.
[15] B. Després, Weak consistency of the cell-centered Lagrangian GLACE scheme on general meshes in any dimension, *Comput. Methods Appl. Mech. Eng.*, 199(41):2669–2679, 2010.
[16] B. Després and F. Lagoutière, Numerical resolution of a two-component compressible fluid model with interfaces, *Prog. Comput. Fluid Dyn.*, 7(6):295–310, 2007.
[17] P. Drake, E. Myra, M. J. Grosskopf, E. Rutter, and B. Torralva, Behavior of irradiated low-Z walls and adjacent plasma, in: *APS Division of Plasma Physics Meeting Abstracts*, Vol. 52, APS, NP9–053, 2010.
[18] D. A. Drew, Mathematical modeling of two-phase flow, *Annu. Rev. Fluid Mech.*, 15(1):261–291, 1983.
[19] F. Duboc, C. Enaux, S. Jaouen, H. Jourdren, and M. Wolff, High-order dimensionally split Lagrange-Remap schemes for compressible hydrodynamics, *C. R. Math.*, 348(1):105–110, 2010.
[20] S. Galera, P.-H. Maire, and J. Breil, A two-dimensional unstructured cell-centered multi-material ALE scheme using VOF interface reconstruction, *J. Comput. Phys.*, 229(16):5755–5787, 2010.
[21] R. V. Garimella, V. Dyadechko, B. K. Swartz, and M. J. Shashkov, Interface reconstruction in multi-fluid, multi-phase flow simulations, in: *Proceedings of the 14th International Meshing Roundtable*, Springer, 19–32, 2005.
[22] P. Hergibo, T. N. Phillips, and Z. Xie, A moment-of-fluid method for resolving filamentary structures using a symmetric multi-material approach, *J. Comput. Phys.*, 491:112401, 2023.
[23] É. Heulhard de Montigny and A. Llor, Taming the "stiff stiffness" of pressure work and equilibration in numerical schemes for compressible multi-fluid flows, *Int. J. Multiph. Flow*, 153:104078, 2022.
[24] C. Hirt, A. A. Amsden, and J. L. Cook, An arbitrary Lagrangian-Eulerian computing method for all flow speeds, *J. Comput. Phys.*, 14(3):227–253, 1974.
[25] M. Ishii, *Thermo-Fluid Dynamic Theory of Two-Phase Flow*, in: *Collection de la Direction des Études et Recherches d'Electricité de France*, Vol. 22, Eyrolles, 1975.
[26] A. Kapila, R. Menikoff, J. Bdzil, S. Son, and D. Stewart, Two-phase modeling of deflagration-to-detonation transition in granular materials: Reduced equations, *Phys. Fluids*, 13:3002–3024, 2001.
[27] E. Kikinzon, Y. Kuznetsov, K. Lipnikov, and M. Shashkov, Approximate static condensation algorithm for solving multi-material diffusion problems on meshes non-aligned with mate-

rial interfaces, *J. Comput. Phys.*, 347:416–436, 2017.
[28] E. Kikinzon, M. Shashkov, and R. Garimella, Establishing mesh topology in multi-material cells: Enabling technology for robust and accurate multi-material simulations, *Comput.* & Fluids, 172:251–263, 2018.
[29] P. G. LeFloch and S. Mishra, Numerical methods with controlled dissipation for small-scale dependent shocks, *Acta Numer.*, 23:743–816, 2014.
[30] W. Li, C. Liu, Y. Zhu, J. Zhang, and K. Xu, Unified gas-kinetic wave-particle methods III: Multiscale photon transport, *J. Comput. Phys.*, 408:109280, 2020.
[31] R. Loubère, P.-H. Maire, and B. Rebourcet, Staggered and colocated finite volume schemes for Lagrangian hydrodynamics, in: *Handbook of Numerical Methods for Hyperbolic Problems: Basic and Fundamental issues*, 17:319–352, 2016.
[32] P.-H. Maire, R. Abgrall, J. Breil, and J. Ovadia, A cell-centered Lagrangian scheme for two-dimensional compressible flow problems, *SIAM J. Sci. Comput.*, 29(4):1781–1824, 2007.
[33] B. Manach-Pérennou, R. Chauvin, S. Guisset, and A. Llor, Cell-centered Lagrangian scheme for multi-material flows with pressure equilibration, *Comput.* & *Fluids*, 250:105705, 2023.
[34] R. Menikoff and B. J. Plohr, The Riemann problem for fluid flow of real materials, *Rev. Mod. Phys.*, 61:75–130, 1989.
[35] D. Mihalas and B. Mihalas, *Foundations of Radiation Hydrodynamics*, Oxford University Press, 1964.
[36] V. A. Mousseau and D. A. Knoll, Temporal accuracy of the nonequilibrium radiation diffusion equations applied to two-dimensional multimaterial simulations, *Nucl. Sci. Eng.*, 154(2):174–189, 2006.
[37] B. J. Parker and D. L. Youngs, *Two and Three Dimensional Eulerian Simulations of Fluid Flow with Material Interfaces*, Technical Report, Atomic Weapons Establishment, 1992.
[38] M. Petrella, R. Abgrall, and S. Mishra, On the discrete equation model for compressible multiphase fluid flows, *J. Comput. Phys.*, 478:111974, 2023.
[39] D. P. Starinshak, *Level Set Methods for Multimaterial Radiative Shock Hydrodynamics*, PhD Thesis, University of Michigan, 2012.
[40] P. D. Thomas and C. K. Lombard, Geometric conservation law and its application to flow computations on moving grids, *AIAA J.*, 17(10):1030–1037, 1979.
[41] P. Woodward and P. Colella, The numerical simulation of two-dimensional fluid flow with strong shocks, *J. Comput. Phys.*, 54(1):115–173, 1984.
[42] M. Wörner, *A Compact Introduction to the Numerical Modeling of Multiphase Flows*, Vol. 6932, FZKA, 2003.
[43] I. B. Zeldovich and Y. P. Raizer, *Physics of Shock Waves and High-Temperature Hydrodynamic Phenomena*, Academic Press, 1966.